

# HerEOS: A framework for consistent treatment of the Equation of State in ALE hydrodynamics

Michal Zeman<sup>a</sup>, Milan Holec<sup>b</sup>, Pavel Váchal<sup>a,\*</sup>

<sup>a</sup> Faculty of Nuclear Sciences and Physical Engineering, Czech Technical University in Prague, Břehová 7, 115 19 - Praha 1, Czech Republic

<sup>b</sup> Université de Bordeaux - CNRS - CEA, CELIA, UMR 5107, F-33405 Talence, France



## ARTICLE INFO

### Article history:

Available online 1 November 2018

### Keywords:

Equation of State  
Thermodynamic consistency  
Helmholtz free energy  
Hermite interpolation

## ABSTRACT

We propose a general methodology and practical implementation of arbitrary Equations of State (EOS) evaluation for Lagrangian and ALE hydrodynamic simulations. This approach is based on higher-order interpolations of the Helmholtz free energy (HFE) and derived quantities. We also discuss several pitfalls related to thermodynamic consistency, physical relevance and robustness of the EOS calculations and demonstrate them for realistic values of temperature and density. The developed library HerEOS has been tested and used in various hydrodynamic codes for practical laser plasma simulations, some of which are presented here.

© 2018 Elsevier Ltd. All rights reserved.

## 1. Introduction

One of the most challenging issues we face in the simulations of hydrodynamics and laser-plasma interactions is the hydrodynamic closure and proper evaluation of the Equation of State (EOS). To get realistic results that are in good correspondence with experimental data, we have to use physically relevant EOS. Depending on particular range of parameters such as density, temperature and laser intensity, we might need to use various physical models and thus various EOS, sometimes even combine them in one simulation. Among the many existing EOS models and libraries varying in primary purpose, complexity and availability, we generally encounter two types. In the simpler (“inline”) case, such as for QEOS [1]/FEOS [2], one can directly obtain values for pressure, internal energy, entropy, and other thermodynamic quantities at any point (say in the temperature–density space), but the calculation may be expensive. EOS of the other type, such as the Los Alamos library SESAME [3], are based on theoretical models combined with experimental data and provided only as discrete values of state variables, with the distribution of data far from ideal. At this point let us remark, that some EOS combine inline and tabulated approaches for different regions.

Our objective here is to develop a tool that allows fast and consistent evaluation of various Equations of State including (but not limited to) ideal polytropic gas, QEOS [1], MPQeos [4], FEOS [2], BADGER [5], and SESAME [3]. This tool, which we will refer to as HerEOS (Hermite-interpolated Equation of State), is intended as a standalone module to be used with various multi-dimensional simulation codes. So far, we have tested our implementation with the 2D Arbitrary Lagrangian–Eulerian code PALE [6] and the multi-dimensional Lagrangian code PETE (Plasma Euler and Transport Equations) [7,8].

Among several reasons to develop such an instrument is the need to reduce the computational cost. In practice, analytical (inline) calculation of a typical EOS, such as QEOS, involves repeated evaluation of complicated formulas and solution of implicit equations leading to the computationally demanding inverse problems. A substantial speed-up can be achieved

\* Corresponding author.

E-mail address: [pavel.vachal@fjfi.cvut.cz](mailto:pavel.vachal@fjfi.cvut.cz) (P. Váchal).

by pre-calculation of tables and interpolation from these in the actual simulation. In order to provide consistent data, our method precisely obeys fundamental thermodynamic relations between thermodynamic potentials and derived quantities referred to as *thermodynamic consistency*. This is not always the case in existing EOS libraries, where a limited set of thermodynamic quantities, such as pressure and internal energy, is typically provided without any care about their mutual physical dependences. This fact is particularly problematic in the case of tabulated EOS.

To ensure the desired properties and preserve consistency (to be detailed below), we follow the idea of Timmes and Swesty [9,10] and perform a high-order piecewise Hermite-type interpolation of the Helmholtz free energy (a thermodynamic potential dependent on density and temperature), which we will refer to as *thermodynamic interpolation* throughout this text. The actual interpolation uses pre-calculated tabulated values of the Helmholtz free energy and its derivatives. These are either calculated by finite differencing from the free energy, or obtained from the values of derived quantities, e.g., from pressure or internal energy.

The rest of this paper is organized as follows. Section 2 contains an overview and explanation of thermodynamic properties which the developed method should possess regarding the physical relevance, the thermodynamic consistency and the computational cost, and mentions some difficulties related to the fulfillment and the enforcement of these requirements. Section 3 gives a brief description of existing methods, explains how Hermite-type interpolation can be employed, suggests its particular implementation in the HerEOS library and comments on its desirable properties. Selected realistic hydrodynamic simulations of laser-heated plasma using HerEOS as the EOS module are shown in Section 4. Finally, Section 5 contains practical examples of some non-physical behavior and inconsistencies of the data provided by existing EOS libraries. Let us stress, that this last part is not meant as a criticism of the respective EOS libraries, most of which are very useful and provide realistic results in many situations, but rather as a demonstration of issues which are often encountered in practice and should be avoided or at least taken into account when working with popular Equations of State in the hydrodynamic simulations of plasma. We are placing this section at the very end rather than concluding the text with the successful results given in Section 4, in order to stimulate discussion about open questions, and possibly some follow-up work.

## 2. Thermodynamic consistency of EOS

The Euler equations of Lagrangian hydrodynamics

$$\frac{d\rho}{dt} = -\rho \nabla \cdot \mathbf{v}, \quad (1)$$

$$\rho \frac{d\mathbf{v}}{dt} = -\nabla (p_e + p_i) + \nabla \cdot \mu \sigma, \quad (2)$$

$$\rho \frac{d\varepsilon_e}{dt} = -p_e \nabla \cdot \mathbf{v} - \nabla \cdot \mathbf{q}_H - \nabla \cdot \mathbf{q}_S, \quad (3)$$

$$\rho \frac{d\varepsilon_i}{dt} = (\mu \sigma - p_i \mathbf{I}) : \nabla \mathbf{v}, \quad (4)$$

where  $\rho$  is the density,  $\mathbf{v}$  the fluid velocity,  $p_e, p_i$  the pressure of electrons and ions, and  $\varepsilon_e, \varepsilon_i$  their internal energy, represent one of the most successful plasma models on macroscopic scale. The viscous extension of these equations resides in parabolic terms represented by viscosity  $\mu$ , symmetrized velocity gradient  $\sigma = \frac{1}{2}(\nabla \mathbf{v} + \mathbf{v} \nabla)$ , and electron heat flux  $\mathbf{q}_H$  given by the heat conduction

$$\rho c_{Ve} \frac{dT_e}{dt} = -\nabla \cdot \mathbf{q}_H, \quad (5)$$

$$\mathbf{q}_H = -\kappa_e \nabla T_e, \quad (6)$$

where  $T_e$  is the temperature of electrons,  $c_{Ve}$  the specific heat capacity at constant volume, and  $\kappa_e$  the heat conductivity. The term  $-\nabla \cdot \mathbf{q}_S$  in (3) provides a general source of energy, e.g., the laser energy deposition.

The key role of the Equation of State in (1)–(6) resides in providing the physical properties of plasma, i.e., the Equation of State closure

$$p_e(T_e, \rho), \quad p_i(T_i, \rho), \quad \varepsilon_e(T_e, \rho), \quad \varepsilon_i(T_i, \rho), \quad \mu(T_e, T_i, \rho), \quad c_{Ve}(T_e, \rho), \quad \kappa_e(T_e, \rho), \quad (7)$$

where the dependence on density  $\rho$ , electron temperature  $T_e$ , and ion temperature  $T_i$  is considered. This is in agreement with the dependence of the Helmholtz free energy of electrons and ions, i.e.,  $f_e(T_e, \rho)$  and  $f_i(T_i, \rho)$ , respectively. Since the primary variables of hydrodynamic equations (1)–(4) is the set  $(\rho, \mathbf{v}, \varepsilon_e, \varepsilon_i)$ , the inverse evaluations

$$T_e(\rho, \varepsilon_e), \quad T_i(\rho, \varepsilon_i) \quad (8)$$

must also be provided in order to consequently evaluate the EOS closure (7) and heat conduction (5) and (6).

Even though it is not explicitly used in hydrodynamic simulations, it is worth mentioning that all the thermodynamic quantities can be written as functions of free energy, that is,

$$p_e(f_e(T_e, \rho)), \quad p_i(f_i(T_i, \rho)), \quad \varepsilon_e(f_e(T_e, \rho)), \quad \varepsilon_i(f_i(T_i, \rho)), \quad \mu(f_e(T_e, \rho), f_i(T_i, \rho)), \quad c_{Ve}(f_e(T_e, \rho)), \quad (9)$$

which makes them inherently dependent, e.g., see Eq. (18), and the resulting action of the Equation of State in hydrodynamics exhibits properties of the thermodynamic consistency.

### 2.1. The Helmholtz free energy

We require correct relations to hold between the state variables and their derivatives. In this text, we consider all variables in their specific form (that is, per mass) as functions of temperature  $T$  and density  $\rho$ .

A fundamental thermodynamic quantity is the Helmholtz free energy (HFE)  $f(T, \rho)$ , which is used to express the basic thermodynamic quantities in hydrodynamics, in particular specific entropy

$$s(T, \rho) = - \left( \frac{\partial f}{\partial T} \right)_{\rho}, \quad (10)$$

specific internal energy

$$\varepsilon(T, \rho) = f + T s = f - T \left( \frac{\partial f}{\partial T} \right)_{\rho} \quad (11)$$

and pressure

$$p(T, \rho) = \rho^2 \left( \frac{\partial f}{\partial \rho} \right)_T. \quad (12)$$

Useful derived quantities include the specific isochoric heat capacity

$$c_v(T, \rho) = \left( \frac{\partial \varepsilon}{\partial T} \right)_{\rho} = T \left( \frac{\partial s}{\partial T} \right)_{\rho} = -T \frac{\partial^2 f}{\partial T^2} \quad (13)$$

and the adiabatic speed of sound

$$\begin{aligned} c_s(T, \rho) &= \sqrt{\left( \frac{\partial p}{\partial \rho} \right)_s} = \sqrt{\frac{c_p}{c_v} \left( \frac{\partial p}{\partial \rho} \right)_T} = \sqrt{\frac{c_p}{c_v} \frac{\partial}{\partial \rho} \left( \rho^2 \frac{\partial f}{\partial \rho} \right)} \\ &= \sqrt{2\rho \left( \frac{\partial f}{\partial \rho} \right)_T + \rho^2 \left( \frac{\partial^2 f}{\partial \rho^2} \right)_T - \rho^2 \left( \frac{\partial^2 f}{\partial T^2} \right)_{\rho}^{-1} \left( \frac{\partial^2 f}{\partial T \partial \rho} \right)^2}, \end{aligned} \quad (14)$$

with  $c_p$  being the isobaric heat capacity. These relations are illustrated in [Appendix A](#) on the simple case of a mono-atomic ideal gas. The thermodynamic quantities originally arise from the HFE differential

$$df = -s dT + \frac{p}{\rho^2} d\rho, \quad (15)$$

which represents one of the formulations of the first law of thermodynamics.

The Helmholtz free energy is a potential, which essentially means that

$$\frac{\partial^2 f}{\partial T \partial \rho} = \frac{\partial^2 f}{\partial \rho \partial T}, \quad (16)$$

or, equivalently,

$$\frac{\partial p}{\partial T} = -\rho^2 \frac{\partial s}{\partial \rho}, \quad (17)$$

resp. for pressure and internal energy

$$p - T \frac{\partial p}{\partial T} = \rho^2 \frac{\partial \varepsilon}{\partial \rho}. \quad (18)$$

This also ensures that internal energy is a potential. Preserving this property of thermodynamic potentials in numerical calculations is important and, as we will see later, it can be achieved by using a sufficiently high order of interpolation. Unfortunately, some existing methods fail to do so – for example, using a non-potential function for internal energy leads to the violation of thermodynamic laws. That is, some work could be done on the system without changing the internal energy (under constant heat), which is physically a nonsense.

From the above, it is easy to conclude, that there is a strict relation among the thermodynamic quantities used in hydrodynamics, e.g., between pressure and internal energy. Failure to obey these dependences leads to inconsistencies and may lead to physically incorrect results and even numerical difficulties, as will be shown later.

### 2.2. General physical requirements on EOS

At this point, let us mention some basic constraints on the values of thermodynamic variables. Some of them are obvious, some are consequences of the thermodynamic requirements from Section 2.1. We definitely require non-negative fluid

pressure<sup>1</sup> and heat capacity (isochoric as well as isobaric),  $p \geq 0$ ,  $c_V \geq 0$ ,  $c_p \geq 0$ , and real (non-complex) speed of sound,  $c_s \in \mathbb{R}^+$ . Here we also want the entropy to be non-negative,  $s \geq 0$ . This leads to a very fundamental physical argument, that the Helmholtz free energy of the system should be minimized for maximum entropy (11). Correspondingly, we also require that  $\varepsilon(0, \rho) = f(0, \rho)$ .

Translating this to Helmholtz free energy  $f$ , these basic requirements are met when

- HFE is monotonically increasing in density to provide non-negative pressure,  $p \geq 0$  (12), and we also want it to be monotonically decreasing in temperature, thus providing non-negative entropy,  $s \geq 0$  (10).
- HFE is concave in temperature,  $\frac{\partial^2 f}{\partial T^2} \leq 0$ , which ensures non-negative heat capacity,  $c_V = \frac{\partial \varepsilon}{\partial T} \geq 0$ , and entropy monotonically increasing in temperature,  $\frac{\partial s}{\partial T} \geq 0$ , see (13) and (10).
- HFE satisfies  $\frac{\partial}{\partial \rho} \left( \rho^2 \frac{\partial f}{\partial \rho} \right) \geq 0$ , that is, pressure is monotonically increasing in density,  $\frac{\partial p}{\partial \rho} \geq 0$ , in order to provide a positive speed of sound ( $c_s \in \mathbb{R}^+$ ), see (14).

### 3. The HerEOS framework

#### 3.1. State of the art

Assume we have the EOS given by discrete values of thermodynamic quantities such as HFE, pressure or internal energy on a rectangular grid in the temperature–density space and we want to get the values at a general point  $(T, \rho)$ . The most straightforward approach, used as the first choice in the literature, is to reconstruct each of these quantities by linear (dimensionally split) or bilinear interpolation on each bin (cell of the  $T$ – $\rho$  space), which we will refer to as bilinear *direct interpolation*. The attribute *direct* means that the interpolation technique is directly applied to the discrete data of one given quantity, e.g., pressure. Among the drawbacks of this really simple and numerically robust method are discontinuous derivatives on the bin boundaries, which cause numerical issues as well as physical inconsistencies. Thermodynamic quantities are particularly difficult to approximate, for example near the phase transitions with steep gradients, and thus methods such as higher-order Lagrange interpolations or splines suffer from spurious oscillations. A nice review of this, motivated by the work with SESAME EOS, can be found in [11], where the authors also suggest to replace the interpolating polynomials by rational functions. While this approach indeed significantly improves the results in many cases, it still does not worry about the thermodynamic consistency and other physical requirements from Sections 2.1 and 2.2. For example, as can be seen in (13), isochoric heat capacity can be calculated in various ways, which are theoretically equivalent, but in practice can give different results, depending on which numerical interpolation method is used to interpolate internal energy, entropy or HFE, and how the derivatives are calculated. Similarly, interpolating directly the discrete values of pressure and of internal energy does not ensure the existence of HFE that would even approximately satisfy (12) and (11) at the same time. From this viewpoint it seems reasonable to interpolate only one state variable, e.g. the Helmholtz free energy, and derive the others in a consistent way. We refer to this approach as the *thermodynamic interpolation*.

#### 3.2. Consistent and efficient Hermite interpolation of a general EOS

In what follows, we describe the algorithm in which the Hermite *thermodynamic interpolation* is used to consistently evaluate a general (i.e., any) EOS, based on discrete values of the following thermodynamic quantities:

$$f, \quad p, \quad \varepsilon, \quad \frac{\partial p}{\partial \rho}, \quad \frac{\partial \varepsilon}{\partial T}, \quad \frac{\partial p}{\partial T}, \quad \frac{\partial \varepsilon}{\partial \rho}. \quad (19)$$

Higher-order derivatives can also be employed, depending on the order of the interpolation being constructed.

There are two basic situations: inline EOS and tabulated EOS. In the case of tabulated EOS, the *thermodynamic interpolation* approach provides some additional physical properties, which are usually omitted in hydrodynamic simulations with the EOS closure supplied by bilinear *direct interpolation*.

In other words, we want to evaluate the EOS while enforcing physical sanity and the inter-relations (10)–(16). In the case of an inline EOS library, which we believe to provide consistent quantities, this interpolation serves mainly to accelerate the evaluation. However, in practice many of the dependences ensuring EOS consistency are ignored in existing inline EOS implementations (based on analytical formulas). Thus for these latter libraries, we want to substantially accelerate the evaluation of EOS while preserving the same accuracy as with inline calculations, and moreover satisfy all the above physical and thermodynamic constraints.

We suggest a method based on the idea from [9,10]: Reconstruct one basic state variable (in our case HFE) by local Hermite-type interpolation of sufficient order. In one dimension, the Hermite interpolation is a method to approximate

<sup>1</sup> Based on our experience in hydrodynamic simulations with a two-temperature model, we believe that the possible use of negative electron pressure could be highly favorable in laser-heated plasma simulations. In particular, this could properly handle the pressure of a cold solid state corresponding to the initial state of simulated material, ensuring that the total pressure is zero and the material remains at rest until the effect of laser energy applies. However, this trick, referred to as “semiempirical correction for chemical bonding” in [1], will not be applied in this text. To keep it simple, here we require positive pressure of ions as well as of electrons.

a general function  $f(x)$  on interval  $[x_0, x_1]$  by a simple polynomial function such, that the approximating function's values as well as derivatives up to a certain order at the endpoints  $x_0$  and  $x_1$  agree with those of the original function. This approach can be used to approximate a complicated function by a simple polynomial, using also intermediate points between  $x_0$  and  $x_1$ , or to reconstruct an unknown function from its known values and derivatives at the endpoints. In the latter case, the one-dimensional Hermite interpolation only uses two (end-)points, which substantially simplifies the situation. In our particular application, we will reconstruct the Helmholtz free energy on a quadrilateral in the 2D temperature–density space solely from the values and derivatives of HFE at the four corners (vertices). This is why we also refer to the method as to “local Hermite-type interpolation”.

To repeat, we will reconstruct a function (in our case the Helmholtz free energy) from its known values and derivatives at discrete points in the  $T$ - $\rho$  space. To get these input data, we can follow two approaches: either use the provided EOS only to acquire HFE inline and then calculate the derivatives (needed to construct the *thermodynamic interpolation*) by finite differences; or directly pull from the EOS library also other quantities (such as pressure or internal energy) and use them to calculate the needed derivatives of HFE according to relations (10)–(14) and their analogs. Both approaches should be equivalent when the EOS involved is consistent, however, very often it is not the case. In practice, in the latter case consistency of HFE with other quantities provided by EOS must be checked, using e.g. the aforementioned finite differences. Except for simple cases such as ideal gas, where everything works as expected, in real EOS the variables often turn out to be highly inconsistent even after a brief visual check! One of the possible reasons is the fact, that the tabulated EOS are typically created by a combination of experimental measurements and post-processing, so that for example some variables are given as raw data while others have been calculated using numerical integration, interpolation, smoothing, etc.

To ensure the thermodynamic consistency – see especially (16), (18), (13) and (14) – the interpolation should be at least bicubic, which also provides numerically useful properties such as continuous derivatives of pressure and energy. In [9,10], biquintic interpolation is suggested in order to ensure additional physical and numerical properties.

Unfortunately, the higher order of the interpolation is used, the more sensitive is the result to the consistency of provided data. As we will demonstrate on practical examples in Section 5, in some cases the errors due to inconsistencies in the EOS library on input override the gain of obeying proper physical requirements, and render the high-order interpolation useless. In this case, one either has to resort to a direct lower-order interpolation (and thus give up full thermodynamic consistency, as most current interpolation-based methods do), or try to automatically detect and correct these inconsistencies by preprocessing, possibly utilizing also the useful ideas from [11]. The latter option is still work in progress and is beyond the scope of this text.

### 3.3. The HerEOS code

At this point let us present the actual implementation of our HerEOS code and some of its properties.

#### 3.3.1. Part I: Initialization

Before the actual simulation starts, we have to prepare the interpolation tables, that is, data from which the actual interpolation will be performed later in the course of the simulation. Most importantly, we need the values of Helmholtz free energy and its derivatives up to desired order at given points in the temperature–density space. This is done just once as a preprocessing step for a given EOS and for the expected range of data, and these tables can be stored for reuse with future simulations, with no need to recalculate them over and over.

If the EOS is provided as discrete values of state variables on a given grid in the  $T$ - $\rho$  space, we simply reuse this grid and load available variables. Typically, the grid is logically rectangular, but the spacing is not always ideal for interpolation, since (to our knowledge) it was often chosen to capture physical behavior of given material at certain conditions. In most cases, the values of HFE are given. The values of its derivatives at the grid points (in the  $T$ - $\rho$  space) up to the specified order can be either calculated from the other provided variables using relations (10)–(14), for example first partial derivatives from pressure and internal energy, or calculated by finite differencing. Typically, especially for higher-order interpolations, a combination of both approaches is used: available values of derived variables are used and the rest is calculated by finite differences. At this point, some of the most obvious nonphysical values and variable inconsistencies can be captured and corrected, as we already mentioned earlier.

For EOS given as inline functions, that is, when the provided library returns the variables for any temperature and density from the region of interest, we construct the  $T$ - $\rho$  grid as we need, with desired range, spacing and distribution. Typically we use a rectangular grid with linear or logarithmic spacing. Then we generate on this grid the values of HFE and its derivatives up to the order needed by the *thermodynamic interpolation*, again using either the values of derived variables or finite differencing. Combining these two approaches, we can discover even more inconsistencies than we did in the case of discrete EOS.

To rephrase, in this initialization part of the algorithm, we are transferring the data from an externally provided EOS onto the interpolation grid in the  $(T$ - $\rho)$  space. For example, for the bicubic interpolation, we need the values of variables listed in (19). Out of these, HFE is almost always given, and typically also pressure and internal energy. The others are sometimes provided, sometimes have to be calculated using finite differences, the relations from Section 2.1, and/or the values of further available quantities such as heat capacities. Sometimes, especially when we suspect serious inconsistency in the EOS library on input, we may even opt to replace the use of provided pressure and/or internal energy values by finite differencing of

HFE. To avoid introducing further errors in the case of discrete EOS, we prefer to use the provided data as they are, that is, keep their original grid (in  $T$ - $\rho$  space) and reuse it as our interpolation grid, rather than selecting just some points or pre-interpolating the data to create a more dense or regular interpolation grid. Note that in this way, no matter if we work with inline or discrete EOS, the only error introduced at this initialization stage may come from finite differencing. However, (so far) at this point we do not cure all physical and thermodynamic inconsistencies contained in the data provided by the source EOS library. These inconsistencies are unfortunately often rather serious and some of them will be discussed later in Section 5, together with plans to implement some kind of automatic correction into this initialization process in the future.

Let us repeat, that this part is done just once in the very beginning of the simulation (or not at all, if the tables were prepared and stored in previous simulations), so that even if the evaluation of the inline function (or the value sanity checks and consistency repair) is costly, it is not a significant burden for the actual calculation. Moreover, even if the generated  $T$ - $\rho$  grid is relatively fine (and thus the tables for interpolation big), the actual EOS evaluation will consist only of a simple search of the respective bin (cell in  $T$ - $\rho$  space) and a fixed number of operations with the interpolation parameters, so that the computational time will be only very slightly affected.

### 3.3.2. Part II: Actual calculation of hydrodynamic quantities by interpolation

In the actual simulation, each evaluation of HFE for given temperature and density consists of finding the appropriate bin (cell of the  $T$ - $\rho$  grid) and computation of the interpolation function from the pre-calculated table. To speed up the calculation, we prefer to have the  $T$ - $\rho$  grid rectangular, but it is not mandatory. Values of the derived quantities can be easily obtained by using corresponding derivatives of the interpolating formula. It is advantageous to calculate all desired quantities for a given  $(T, \rho)$  point at once.

Since the Hermite interpolation is a well known technique, at this point we only give the formula for 2D bicubic interpolation from data on a rectangular  $T$ - $\rho$  grid, which have been prepared in the preprocessing (initialization) step. This is especially simple since we use it here locally, interval per interval, which is what we mean by the term Hermite-style local interpolation. For convenience of the interested reader, we also show in [Appendix B](#) a step-by-step derivation of the biquintic interpolation in 1D.

For a bicubic interpolation on the bin  $[T_{i-1}, T_i] \times [\rho_{j-1}, \rho_j]$ , we need 16 values, which we denote as follows. HFE in the four corners,

$$\begin{aligned} f^{[00]} &= f(T_{i-1}, \rho_{j-1}), & f^{[10]} &= f(T_i, \rho_{j-1}), \\ f^{[01]} &= f(T_{i-1}, \rho_j), & f^{[11]} &= f(T_i, \rho_j), \end{aligned} \quad (20)$$

its partial derivatives w.r.t. temperature

$$\begin{aligned} f_T^{[00]} &= \frac{\partial f}{\partial T}(T_{i-1}, \rho_{j-1}), & f_T^{[10]} &= \frac{\partial f}{\partial T}(T_i, \rho_{j-1}), \\ f_T^{[01]} &= \frac{\partial f}{\partial T}(T_{i-1}, \rho_j), & f_T^{[11]} &= \frac{\partial f}{\partial T}(T_i, \rho_j) \end{aligned} \quad (21)$$

and density

$$\begin{aligned} f_\rho^{[00]} &= \frac{\partial f}{\partial \rho}(T_{i-1}, \rho_{j-1}), & f_\rho^{[10]} &= \frac{\partial f}{\partial \rho}(T_i, \rho_{j-1}), \\ f_\rho^{[01]} &= \frac{\partial f}{\partial \rho}(T_{i-1}, \rho_j), & f_\rho^{[11]} &= \frac{\partial f}{\partial \rho}(T_i, \rho_j) \end{aligned} \quad (22)$$

and mixed derivatives

$$\begin{aligned} f_{T\rho}^{[00]} &= \frac{\partial^2 f}{\partial T \partial \rho}(T_{i-1}, \rho_{j-1}), & f_{T\rho}^{[10]} &= \frac{\partial^2 f}{\partial T \partial \rho}(T_i, \rho_{j-1}), \\ f_{T\rho}^{[01]} &= \frac{\partial^2 f}{\partial T \partial \rho}(T_{i-1}, \rho_j), & f_{T\rho}^{[11]} &= \frac{\partial^2 f}{\partial T \partial \rho}(T_i, \rho_j). \end{aligned} \quad (23)$$

On this interval, we scale temperature and density to unit square

$$t_i(T) = \frac{T - T_{i-1}}{\Delta_i^T}, \quad \Delta_i^T = T_i - T_{i-1}, \quad (24)$$

$$r_j(\rho) = \frac{\rho - \rho_{j-1}}{\Delta_j^\rho}, \quad \Delta_j^\rho = \rho_j - \rho_{j-1} \quad (25)$$

and introduce local auxiliary functions

$$G_k^i(T) = \mathcal{H}_k(t_i(T)), \quad H_k^j(\rho) = \mathcal{H}_k(r_j(\rho)), \quad k \in \{0, 1, 2, 3\}, \quad (26)$$

where  $\mathcal{H}_k$  are cubic Hermite base polynomials

$$\mathcal{H}_0(x) = 1 - 3x^2 + 2x^3, \quad \mathcal{H}_1(x) = x - 2x^2 + x^3,$$



$$\mathcal{H}_2(x) = -x^2 + x^3, \quad \mathcal{H}_3(x) = 3x^2 - 2x^3. \quad (27)$$

(Confront [Appendix B](#) for the derivation and interpretations of  $\mathcal{H}_k(x)$ .) The value of  $f(T, \rho)$  for temperature and density from interval (bin)  $[T_{i-1}, T_i] \times [\rho_{j-1}, \rho_j]$  will now be approximated by the bicubic interpolation function  $\tilde{f}_{ij}(T, \rho)$  defined as

$$\begin{aligned} \tilde{f}_{ij}(T, \rho) = & f^{[00]} G_0^i(T) H_0^j(\rho) + f^{[10]} G_3^i(T) H_0^j(\rho) \\ & + f^{[01]} G_0^i(T) H_3^j(\rho) + f^{[11]} G_3^i(T) H_3^j(\rho) \\ & + f_T^{[00]} G_1^i(T) H_0^j(\rho) \Delta_i^T + f_T^{[10]} G_2^i(T) H_0^j(\rho) \Delta_i^T \\ & + f_T^{[01]} G_1^i(T) H_3^j(\rho) \Delta_i^T + f_T^{[11]} G_2^i(T) H_3^j(\rho) \Delta_i^T \\ & + f_\rho^{[00]} G_0^i(T) H_1^j(\rho) \Delta_j^\rho + f_\rho^{[10]} G_3^i(T) H_1^j(\rho) \Delta_j^\rho \\ & + f_\rho^{[01]} G_0^i(T) H_2^j(\rho) \Delta_j^\rho + f_\rho^{[11]} G_3^i(T) H_2^j(\rho) \Delta_j^\rho \\ & + f_{T\rho}^{[00]} G_1^i(T) H_1^j(\rho) \Delta_i^T \Delta_j^\rho + f_{T\rho}^{[10]} G_2^i(T) H_1^j(\rho) \Delta_i^T \Delta_j^\rho \\ & + f_{T\rho}^{[01]} G_1^i(T) H_2^j(\rho) \Delta_i^T \Delta_j^\rho + f_{T\rho}^{[11]} G_2^i(T) H_2^j(\rho) \Delta_i^T \Delta_j^\rho. \end{aligned} \quad (28)$$

### 3.3.3. Selected properties

Our code HerEOS implements the above described method and as for now works with (contains or calls) several Equations of State, namely ideal polytropic gas (*aka* gamma-law gas), QEOS [1], MPQeos [4], FEOS [2], BADGER [5], and SESAME [3]. Incorporation of further EOS is straightforward. For the future, we also consider to include the possibility to employ raw experimental data from EOS databases such as [12,13].

Formally, all combinations of the interpolation order and the way of derivative calculations are possible, but the most suitable choice for a particular EOS depends on its type, which variables it provides, how consistent these are and what data the simulation code needs on output.

General interfaces for C/C++ and Fortran allow easy linking to any hydrodynamic simulation code — so far it has been tested with the 2D Arbitrary Lagrangian–Eulerian code PALE [6] and the multi-dimensional Lagrangian code PETE (Plasma Euler and Transport Equations) [7,8], which includes the nonlocal transport hydrodynamics for laser plasma modeling and is constructed on the high-order curvilinear finite elements library MFEM [14]. Currently, it is being used as a tool to simply compare results obtained with several different EOS in laser plasma simulations within the same code, which has been seldom done before due to the necessity to access various interfaces and programming languages of the EOS libraries.

As a sanity check, the code has been tested on the simple EOS for ideal polytropic gas, which uses consistent analytical inline formulas. Values interpolated from pre-generated tables converge to analytical (inline) values surprisingly fast, even on very sparse  $T$ – $\rho$  interpolation grids (that is, with small EOS data tables). This is the case for biquintic as well as bicubic *thermodynamic interpolation*. Details are in Section 4.1.

For general inline EOS libraries, even simple calculations with *thermodynamic interpolation* from pre-generated tables are substantially faster than when inline EOS is used directly. A quantified example will be given later in Section 4.2. Any such speed-up is important, since in real physics simulations the evaluation of EOS is usually among the most expensive parts. In larger simulations, an even better speed-up is expected, because the computational cost essentially does not depend on the resolution of the EOS data table used for interpolation. Moreover, using higher order *thermodynamic interpolation* is only slightly more expensive than bilinear *direct interpolation* and provides more state variables, which are typically needed in models incorporating more complex phenomena (such as radiation transport or advanced laser absorption) and would otherwise need to be obtained using additional numerical methods, possibly inconsistent with the EOS in use.

## 4. Numerical results

### 4.1. Convergence of HerEOS to inline EOS

To test the functionality of EOS interpolation by HerEOS in practice, we use a typical simulation of laser–target interaction in the PALE code [6], using the  $r$ – $z$  coordinates. A 40  $\mu\text{m}$  thick Aluminum foil is irradiated by a normally incident 100 J Nd laser pulse (i.e., wavelength  $\lambda = 1053 \text{ nm}$ ) Gaussian in time and space (Full-width-half-maximum  $t_{\text{FWHM}} = 300 \text{ ps}$ , focal spot radius  $r_f = 100 \mu\text{m}$ ). The heated material is ionized and starts to expand in the form of plasma. The process is simulated numerically in cylindrical coordinates, with the symmetry axis of the laser beam corresponding to the  $z$ -axis. To start with, we use a very sparse computational mesh of  $130 \times 140$  cells and the EOS for ideal gas with the heat capacity ratio  $\gamma = 5/3$ . Color maps of density, temperature and the  $z$ -component of velocity at 100 ps after the maximum intensity of the laser are in [Fig. 1](#). Internal energy is not shown, since for the ideal gas it only differs from temperature by a multiplicative factor. The far right plot also shows the computational mesh.

Using the ideal gas EOS is a very raw approximation, and in fact it is not necessary to replace such a simple inline EOS by interpolation, but the purpose of this test is to check how well the HerEOS *thermodynamic interpolation* converges to the solution with inline EOS, depending on the resolution of the interpolation tables in the temperature–density space. To check this for bicubic, resp. biquintic *thermodynamic interpolation*, we need EOS data consistent for derivatives up to the corresponding order, which is why we use the gamma-law gas here.

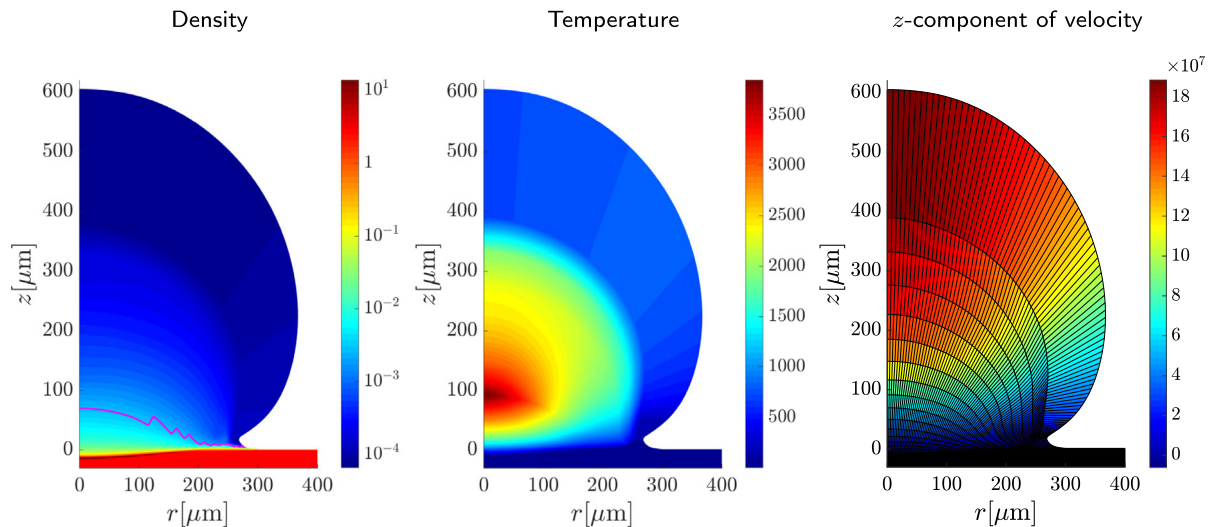


**Fig. 1.** Laser–target interaction at 100 ps after the peak intensity of the pulse. Left: density (logarithmic scale), critical surface by purple line; Center: temperature; Right:  $z$ -component of velocity. Computational mesh shown in the far right plot.

**Table 1**

Convergence of interpolated EOS to inline EOS for ideal gas. Relative discrepancies of density, pressure, temperature and  $z$ -velocity at the location of maximum density.

Number of $T$ - $\rho$ bins	Bicubic				Biquintic			
	$\rho$	$p$	$T$	$u_z$	$\rho$	$p$	$T$	$u_z$
$20 \times 20$	$1.10\text{e-}2$	$7.71\text{e-}2$	$8.90\text{e-}2$	$3.59\text{e-}2$	$9.87\text{e-}3$	$1.71\text{e-}2$	$7.34\text{e-}3$	$4.41\text{e-}3$
$80 \times 80$	$1.92\text{e-}3$	$3.44\text{e-}2$	$3.24\text{e-}2$	$2.36\text{e-}2$	$1.01\text{e-}5$	$2.23\text{e-}5$	$1.21\text{e-}5$	$6.83\text{e-}6$
$320 \times 320$	$8.50\text{e-}6$	$2.02\text{e-}5$	$1.18\text{e-}5$	$4.13\text{e-}6$	$1.29\text{e-}6$	$2.49\text{e-}6$	$1.12\text{e-}6$	$7.11\text{e-}7$

Table 1 shows the convergence of results obtained by interpolated EOS with increasing resolution of the interpolation tables ( $T$ - $\rho$  grid) to the results with inline calculation. In particular, we take the solution at 100 ps after the peak laser intensity, locate the cell with maximum density, and at this place check the relative discrepancy of density, pressure, temperature and the  $z$ -component of velocity w.r.t. the solution obtained using inline EOS. The first column says how dense interpolation grid was used, that is, into how many rectangular bins (with logarithmic spacing) we subdivided the  $T$ - $\rho$  region of interest (with temperatures ranging from  $10^{-3}$  to  $10^4$  eV and density between  $10^{-6}$  and  $10^2$  g cm $^{-3}$ ) to generate the discrete values.

We clearly see that the interpolation-based solution is close to the inline-based solution already with very sparse  $T$ - $\rho$  grids, and that it quickly converges with increasing resolution of *thermodynamic interpolation* tables. This is the case for biquintic as well as bicubic *thermodynamic interpolation*.

Let us repeat, that while generally at least bicubic *thermodynamic interpolation* of HFE should be used for thermodynamic consistency reasons, in practice with real EOS libraries we can encounter situations where severe inconsistency in EOS input data forces us to use some parachute method instead, such as bilinear *direct interpolation* of pressure and internal energy (not of the HFE). This will be discussed later.

#### 4.2. LULI pre-pulse

To demonstrate the effect of various EOS and assess the efficiency of HerEOS, we followed [15] and simulated an experiment for the pre-pulse of the 100 TW LULI laser system in France. An Aluminum target was irradiated by a normally incident 600 ps long (FWHM) laser pulse Gaussian in time as well as space, with peak intensity  $I_{\max} = 5 \times 10^{13}$  W cm $^{-2}$ . The results shown here were obtained by the code PETE [7,8] run in 1D with  $I_{\max}$  (that is, with intensity as on the laser beam axis in the 2D case) up to final time 1400 ps after the laser intensity maximum. Profiles of density and temperature at certain times are in Fig. 2(a). For more details, including the comparison of postprocessed data with the measured values of partial ionization, the reader is referred to [15].

The plots in Fig. 3 show the solution at 500 ps after the intensity peak, as calculated by four different EOS using the HerEOS module. In particular, we compare QEOS, FEOS, SESAME and BADGER. Since some of these EOS are provided by libraries suffering from inconsistency between state variables, we use bilinear *direct interpolation* of pressure and internal energy instead of bicubic *thermodynamic interpolation* of HFE in this test — see Section 5.2 for details and explanation. This



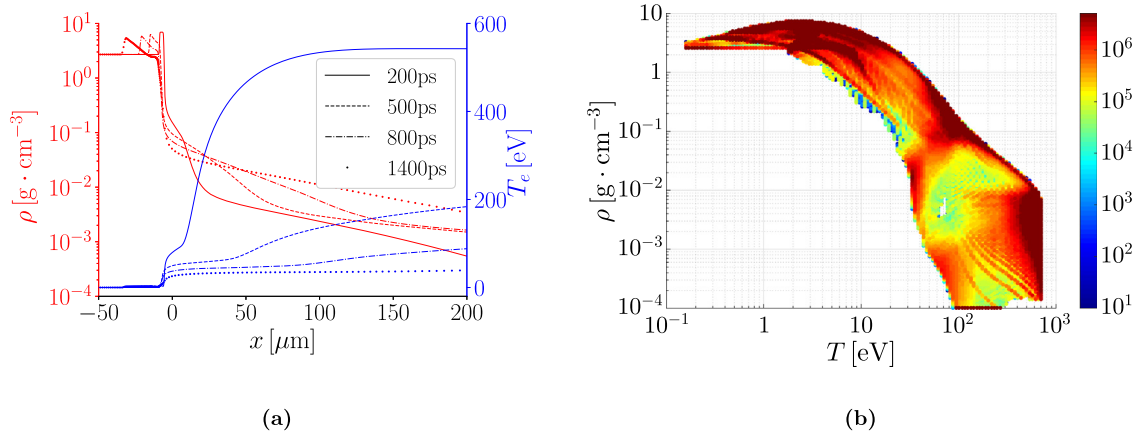


**Fig. 2.** LULI pre-pulse simulation. Left: Aluminum density and temperature at 200, 500, 800 and 1400 ps after the laser intensity peak. Right: Region of  $T$ - $\rho$  space visited throughout the simulation (i.e., where the EOS for electrons was evaluated). Color map shows the number of calls in each bin of the  $T$ - $\rho$  space.

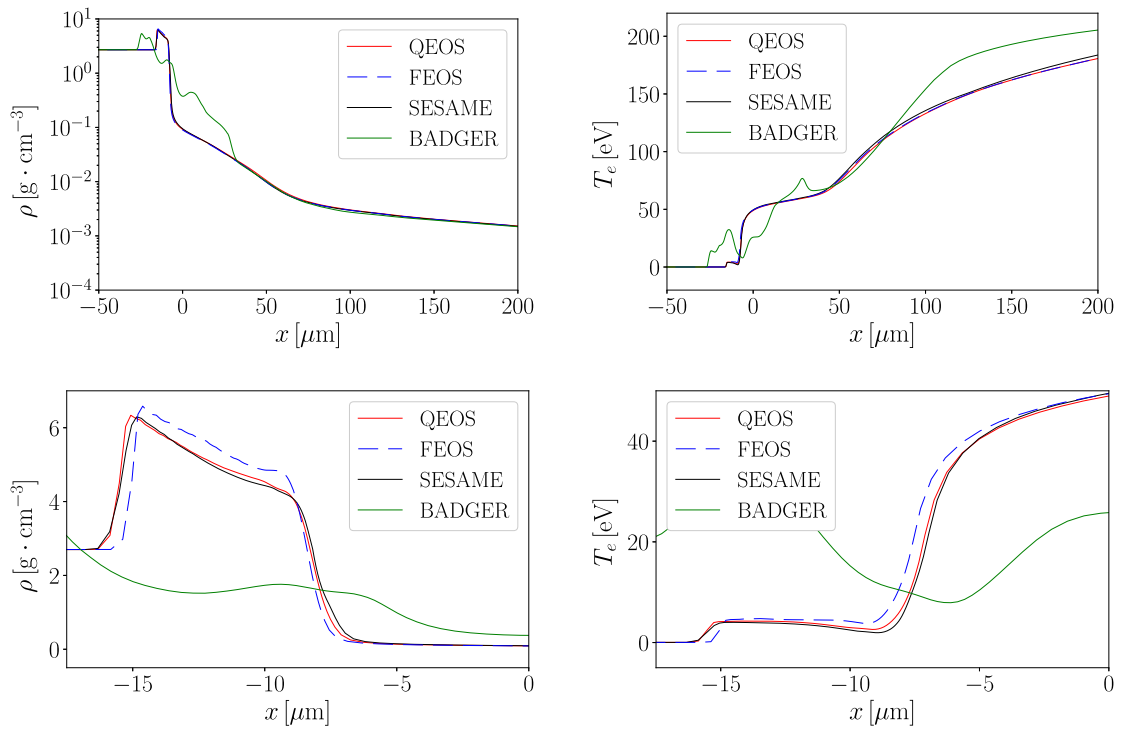


**Fig. 3.** LULI pre-pulse simulation, using the HerEOS tool with various EOS, 500 ps after the laser intensity maximum. Left panel: density on logarithmic scale (top) and detail of density on linear scale (bottom); Right panel: temperature and its detail.

way all the calculations run until completion and we can compare the physical effects of the EOS, abstracting from numerics. Where possible (QEOS, FEOS and BADGER), we tried also inline EOS evaluation, but the results are not shown here, since they are visually identical with those using bilinear *direct interpolation*.

The upper left plot in Fig. 3 shows the density on logarithmic scale. We can see that all tested EOS yield the same basic profile, except for BADGER, which displays behavior irrelevant to our physical model, such as splitting of the wave into two. There is a very good correspondence between QEOS and SESAME results. The difference in density profiles (this time not a logarithm) can be seen in the zoomed-in view in the lower left plot. The right-hand column of Fig. 3 shows the comparison of electron temperature profiles, overall (top) and in detail (bottom).

Now we will take a look at the efficiency of HerEOS. To abstract from the details of the entire complex simulation, let us now focus only on the part performing the actual evaluation of EOS.

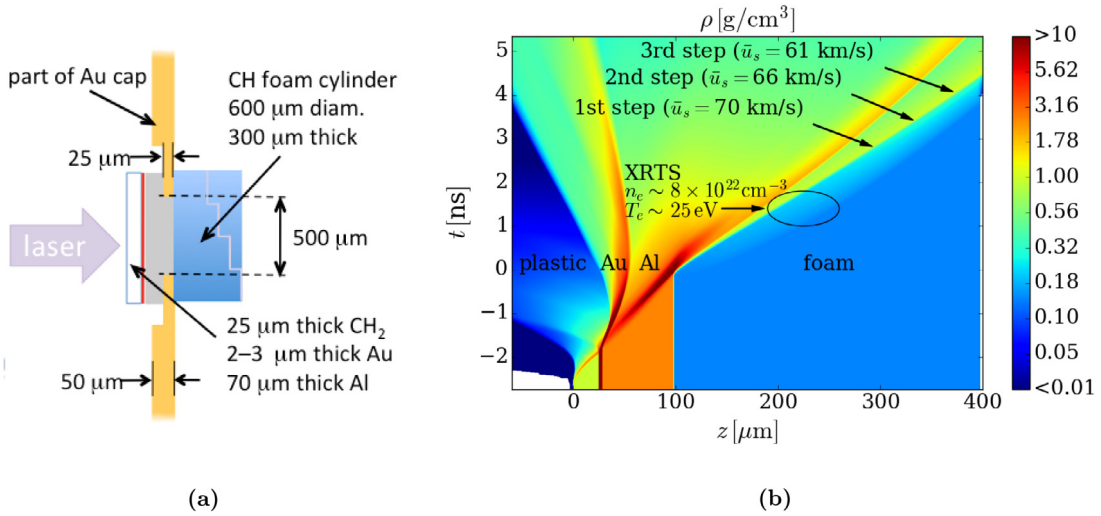


**Fig. 4.** Left: schematic picture of the multi-layer target. Right: results of the PETE simulation of the laser-driven shock wave propagating through the layers of the target.

In particular, we are using time profilers in the code to exactly see how much of the entire simulation time was spent by evaluating the EOS. This provides the real “net time” spent inside EOS for each simulation. However, using various EOS evaluated in various ways leads to slightly different numbers of simulation time steps and requires evaluation at slightly different points in the  $T$ - $\rho$  space. To set a benchmark for comparison of all combinations, we also created a histogram on the region of the  $T$ - $\rho$  space visited throughout the simulation. In Fig. 2(b), the color map describes how many times the corresponding bin (rectangular cell of the  $T$ - $\rho$  space) was accessed in our LULI simulation employing inline FEOS. Then, for each EOS and each evaluation method (inline calls, *direct interpolation* or *thermodynamic interpolation*), we calculate the quantities on each bin as many times as given by the histogram. The total computational times needed for such sampling provide us with the comparison of all methods, focusing only on the “net time” spent by the evaluation of EOS, filtering out the effect of varying costs of the entire simulation. Results obtained by this comparison approach are similar to those of direct profiling and reveal the same qualitative behavior regarding the speed-up of the simulation due to the interpolation of the EOS.

Measured with the sampling approach described just above, the net time of the simulation spent by the evaluation of EOS for electrons at given points of the  $T$ - $\rho$  space was reduced by 23% when inline FEOS calls were replaced by bicubic *thermodynamic interpolation* of HFE, resp. by 60% when bilinear *direct interpolation* of pressure and internal energy was used. As has been said before, an even better improvement can be obtained for more complicated EOS and for simulations using more derived variables. Indeed, FEOS is still cheap compared to other EOS. In our case, replacing inline BADGER by interpolation of BADGER-generated discrete data reduced the cost (“net time”) by 97% (bicubic *thermodynamic interpolation*), resp. by 99% (bilinear *direct interpolation*)!

For completeness, as a hint on what portion of the total simulation time is taken by the evaluation of EOS, let us mention that for example in the simulation with inline FEOS, the “net time” spent in EOS added up to 57% of the total simulation time, while for interpolated SESAME (*directly* or *thermodynamically*) it was 35%, as measured by our time profilers. However, the LULI simulation code at the time of this testing was far from optimized, so we prefer to stick with the comparison of net times.

#### 4.3. Shock velocity in foam at OMEGA

This polystyrene foam hydrodynamic shock experiment was carried out at the OMEGA laser facility at the University of Rochester [16] in order to create warm dense matter conditions and analyze the corresponding Equation of State. Fifteen of the laser beams were overlapped to give a planar  $7 \times 10^{14}$  W cm<sup>-2</sup> square drive with 2 ns duration on  $\lambda = 351$  nm, irradiating a multi-layer target consisting of a 25 μm thick plastic (CH) ablator, 2–3 μm of Au coating used to shield X-ray radiation created at the critical surface of the laser-plasma interaction, a 70 μm Al pusher, and finally 300 μm of C<sub>8</sub>H<sub>8</sub> polystyrene foam. The density of the foam was 0.14 g cm<sup>-3</sup>. The target layout is shown in Fig. 4(a).

The simulation results of the experiment are shown in Fig. 4(b) in the form of a density color map overlaid by some additional data. The laser-driven shock gradually propagating through each of the target layers reaches the foam, where the actual shock velocity is experimentally measured. The thermodynamic conditions in the shock wave traveling through the C<sub>8</sub>H<sub>8</sub> foam were studied with a number of diagnostics developed for the platform including VISAR, SOP and XRTS [17–20]. The shock velocity was measured by an interferometer VISAR system by detecting shock break-out times across four 40 μm

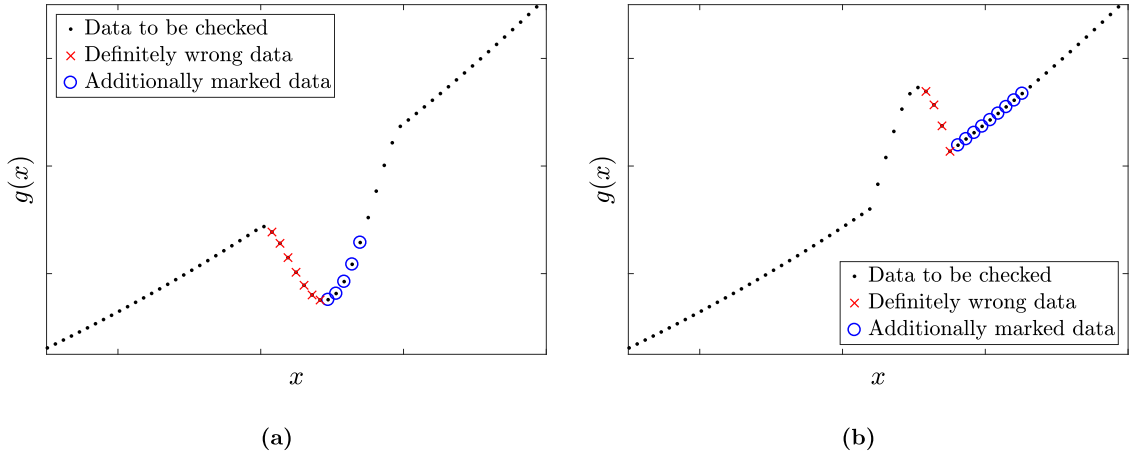


**Fig. 5.** Simple detection of monotonicity violation and its not-so-well working modification. For a perturbation on an increasing function, descending values (red crosses) are surely wrong, but marking also ascending points until the last good value is reached (blue circles) may produce reasonable (left plot) as well as problematic (right plot) output.

steps manufactured on the back side of the target [21]. Independent measurements of shock break-out times were also obtained by the SOP system [22]. The measured shock velocities at the time of break-out were found to be  $57.8 \pm 3.8 \text{ km s}^{-1}$ ,  $64.0 \pm 4.9 \text{ km s}^{-1}$  and  $67.5 \pm 5.0 \text{ km s}^{-1}$ , respectively. Three arrows in the foam layer can be recognized in Fig. 4(b) pointing to the sequence of positions of three steps manufactured on the back side of the target. The simulated shock velocities show a very good agreement compared to experimentally measured shock velocities. We have also performed the Hugoniot jump condition analysis. It has been found that the simulated shock velocity is in excellent agreement with the shock velocity given by SESAME thermodynamic jump conditions at every moment of the shock propagation.

It is worth mentioning, that the foam shock wave exhibits a sign of a finite preheat, which was also observed experimentally by the means of an early SOP emission preceding the VISAR signal [16]. In principle, it is due to the nonlocal electron transport, which is strongly dependent on given temperature and density in the proximity of the shock [7,8]. It was observed, that the Equation of State is absolutely essential for the hydrodynamic simulation, since the values of temperature and density are extremely sensitive to the EOS model used. Even though SESAME tables proved to be a good model in our hydrodynamic simulations, the simplest bilinear *direct interpolation* of pressure and internal energies was finally a mandatory interpolation option, because the *thermodynamic interpolation* strategy presented in Section 3.2 cannot be used due to the inconsistency of provided thermodynamic quantities, in particular the Helmholtz free energy. This issue will be discussed in Section 5.2.

## 5. Issues with existing EOS libraries

Rather than theorizing, we now demonstrate practical issues arising in the calculation with popular EOS libraries on a realistic range of temperature and density. In particular, we focus on the rectangular  $T$ - $\rho$  region with temperature between  $10^{-2}$  and  $10^3 \text{ eV}$  and density between  $10^{-4}$  and  $10 \text{ g cm}^{-3}$ . This choice of range has been inspired by the LULI simulation described in Section 4.2 - the actual region visited by the EOS routine for electrons in that simulation will be demarcated by a green contour within this range in Fig. 13.

### 5.1. Introduction to violations and inconsistencies

Even very simple tests reveal that many existing EOS libraries (inline as well as discrete) do not satisfy the requirements formulated in Section 2.

Consider for example the requirement of monotonicity. Assume there are monotonically increasing discrete data with a dip-shaped local perturbation as in Fig. 5(a). The simplest way to check for wrong data is to flag points whose value is lower than the value of the previous one. Going from left to right, one will find the points highlighted by red crosses. Obviously, there are still some points which are visibly wrong. In this case it appears beneficial and safe to flag as wrong also the following points, marked by blue circles, where the value is still lower than the value at the last good point, that is, than the last value before the decrease started. However, applying this strategy in the case shown in Fig. 5(b), where the perturbation is bump-shaped, does not seem to work well. While crosses correctly flag bad points in the decreasing region, there is visually nothing wrong with the following, circled ones, which the “improved” algorithm would consider wrong. Similarly when proceeding from the other side. While some real improvements can be done to the algorithm, the detection of a problematic region on discrete data representing a generally unknown discrete function will still be more an

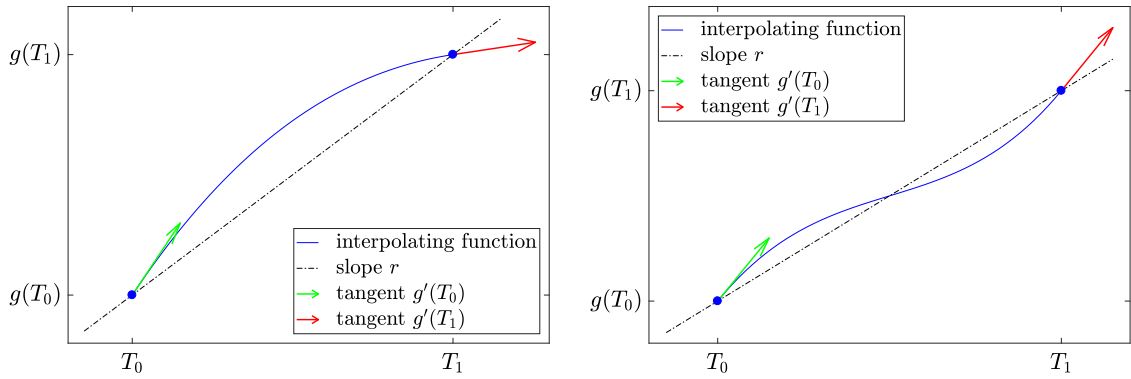


**Fig. 6.** Detection of changes in convexity/concavity of a cubic function on a given interval, based on the derivatives at its endpoints and the slope between them.

approximation than an exact error-bounding procedure. However, even a simple check like the flagging of decreasing values in a function that should theoretically be increasing (red crosses) will detect an issue in existing Equation of State data, as will be shown later.

As for the requirement of concavity of Helmholtz free energy  $f$  in temperature to prevent negative isochoric heat capacity (13), we use a similarly simple detection technique. Assume we want to check the bicubic *thermodynamic interpolation* of  $f(T, \rho)$  along temperature between two points  $(T_0, \rho)$  and  $(T_1, \rho)$  at some fixed density. The available data are values of  $f$  at these endpoints and also its derivatives there, calculated from the values of internal energy  $\varepsilon$  using (11). This is a typical task when working with the SESAME EOS. So, in general, having a 1D cubic function  $g(T)$  between  $T_1$  and  $T_2$  given by its values  $g$  and derivatives  $g'$  at these endpoints, we want to check if the second derivative of function  $g(T)$  changes sign on this interval. Denoting the slope

$$r = \frac{g(T_1) - g(T_0)}{T_1 - T_0}, \quad (29)$$

we see that this cubic function preserves the sign of second derivative if and only if

$$(g'(T_0) - r)(g'(T_1) - r) \leq 0. \quad (30)$$

In the left plot of Fig. 6 is an example where this criterion is satisfied, with the function being concave throughout the interval, while in the right plot the criterion is violated, since the sign of the second derivative is changing.

Again, the situation is more complicated with higher-order *thermodynamic interpolations* and when density and pressure are also taken into account, and in practice also because of possible errors in the values of internal energy and their inconsistency with the data for HFE, but even such a simple test can often discover imperfect regions in some EOS libraries.

Similar inconsistency detection can be also applied for the dependence of HFE on density stated in Section 2.2.

The same technique can be used also for discrete EOS data to detect places where the values of derived variables (pressure, energy, etc.) and consequently of the derivatives of HFE are inconsistent with the discrete values of actual HFE, and thus generate spurious oscillations of the interpolating function, as will be shown in Section 5.2.

## 5.2. Inconsistent values of the Helmholtz free energy

The measure of quality of an EOS for hydrodynamic simulations can be based on the provided quantities such as pressure and internal energy, which should inevitably obey the physical requirements presented in Section 2.2. This is not only for the EOS to provide physically relevant data, but essentially, any violation of these requirements results in an unstable hydrodynamic simulation. In this section we address a not so common topic. That is, the analysis of the provided values of the Helmholtz free energy, which is usually not explicitly used by hydrodynamic codes, but holds the key to the consistent EOS calculations.

The idea of this analysis is very simple. One can check the consistency of the HFE values by integrating over its differential (15) as

$$f(\rho_1, T_1) - f(\rho_0, T_0) = \int_{\rho_0}^{\rho_1} \frac{\partial f}{\partial \rho} d\rho + \int_{T_0}^{T_1} \frac{\partial f}{\partial T} dT = \int_{\rho_0}^{\rho_1} \frac{p}{\rho^2} d\rho - \int_{T_0}^{T_1} s dT, \quad (31)$$

where  $p$  and  $s$  are provided numerically by the EOS. Then, this value of HFE should be consistent with the value of HFE provided by the EOS. Nevertheless, this shows not to be true in many cases, which is shown on several examples for both inline and discrete EOS libraries.

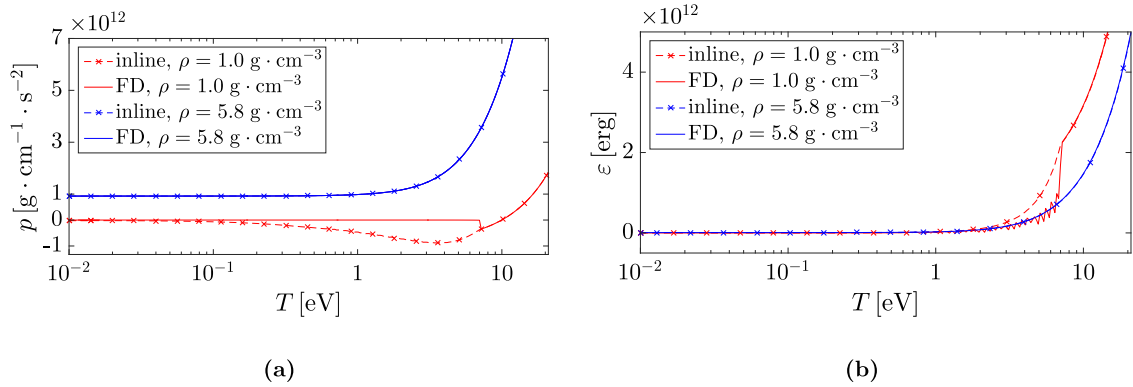


**Fig. 7.** Pressure resp. internal energy by direct inline call of FEOS (dashed) or by finite differences from inline HFE (solid). Pressure (a) is better from HFE than inline. Internal energy (b) is better inline than from HFE.

Apart from the primal issue of the inconsistency of HFE values, one should also consider more refined qualities of the EOS provided HFE, such as whether it is a potential (18), because the first law of thermodynamics must be obeyed without any exception.

#### 5.2.1. The Helmholtz free energy values provided by EOS libraries

In Sections 4.2 and 4.3, the actual hydrodynamic simulations used the bilinear *direct interpolation* exclusively, even though the aim of this work is to provide a consistent *thermodynamic interpolation*. Nevertheless, we had no other choice there, because each of the EOS libraries involved in these tests provided some inconsistent values, in particular, the values of HFE.

In the case of inline EOS library FEOS, this inconsistency can be seen in Fig. 7, showing the dependence of pressure and internal energy on temperature for two different densities, namely  $\rho = 1 \text{ g cm}^{-3}$  (red profiles) and  $\rho = 5.8 \text{ g cm}^{-3}$  (blue). We have actually found an easier way to check (31) by comparing the derivatives of HFE. We compare the calculated HFE derivatives from pressure and internal energy provided by FEOS (dashed lines with cross markers) to the derivatives obtained by applying finite differencing on HFE provided by FEOS (solid lines). This approach is exactly consistent with the numerical integration (31).

In Fig. 7 one can observe, that in the case of lower density (red), the values of both pressure and internal energy provided directly by FEOS differ from values calculated by finite differencing. On the contrary, these values coincide in the case of higher density (blue). In the left panel (a) one can see, that while the direct calls of pressure yield negative values, calculation via HFE avoids sub-zero undershoots almost everywhere, except for a tiny dip near 7 eV. On the other hand, the solid red line in the right panel (b), showing internal energy calculated from HFE, has a jump at this very same temperature, preceded by spurious oscillations starting at about 1 eV. We suspect that the state variables in FEOS routines were corrected here by postprocessing to give better results, but each of them separately, which eventually led to discrepancy between their values in some places.

Note that no interpolation was employed so far in this comparison, just inline EOS and finite differencing.

Unfortunately, the application of *thermodynamic interpolation* on such inconsistent data suffers from spurious oscillations as can be seen in Fig. 8. The upper row shows the dependence of electron pressure on density at temperature 5.5 eV obtained by the interpolation of discrete data generated by inline FEOS on a logarithmic  $T$ - $\rho$  grid. The dashed blue profile in Fig. 8(a) results from bicubic *thermodynamic interpolation* using discrete values of HFE, pressure and internal energy, while for the blue solid line with markers the bicubic *thermodynamic interpolation* was constructed from discrete HFE values and from the values of pressure and energy obtained by finite differencing of inline HFE. For easier understanding we also show inline pressure values (red dashed) and pressure from finite differencing of inline HFE (red solid with markers).

Note that the two red graphs suffer from a similar discrepancy as those in Fig. 7(a). However, at this point we focus on another interesting effect in Fig. 8(a): the significant oscillation in pressure in the case of bicubic *thermodynamic interpolation* using inline pressure and internal energy (blue dashed). We paid a great attention to the origin of these oscillations and we found that these are due to the inconsistency between pressure and HFE values provided by FEOS, where pressure is negative, while HFE is a constant. A corresponding effect on the interpolation of HFE and consequently on pressure can be seen in Fig. 8(c,d). The oscillation of HFE is actually a correct interpolation function, since it matches the constant value of HFE in its discrete points, and also obeys the negative value of its derivative calculated from provided pressure.

The described cause of oscillations of the blue dashed graph is even more obvious in Fig. 8(b), showing the same method with two different interpolation tables. That is, pressure was obtained from bicubic *thermodynamic interpolation* of HFE constructed from discrete values of HFE, pressure and energy, using different grids in  $T$ - $\rho$  space where the data were given. In particular, for the blue graph the entire domain ( $T \in [10^{-2}, 10^3] \text{ eV}$ ,  $\rho \in [10^{-4}, 10] \text{ g cm}^{-3}$ ) was covered by a rectangular grid of  $25 \times 25$  points with logarithmic spacing, while the red graph was obtained from a  $50 \times 50$  grid. It can be clearly seen,

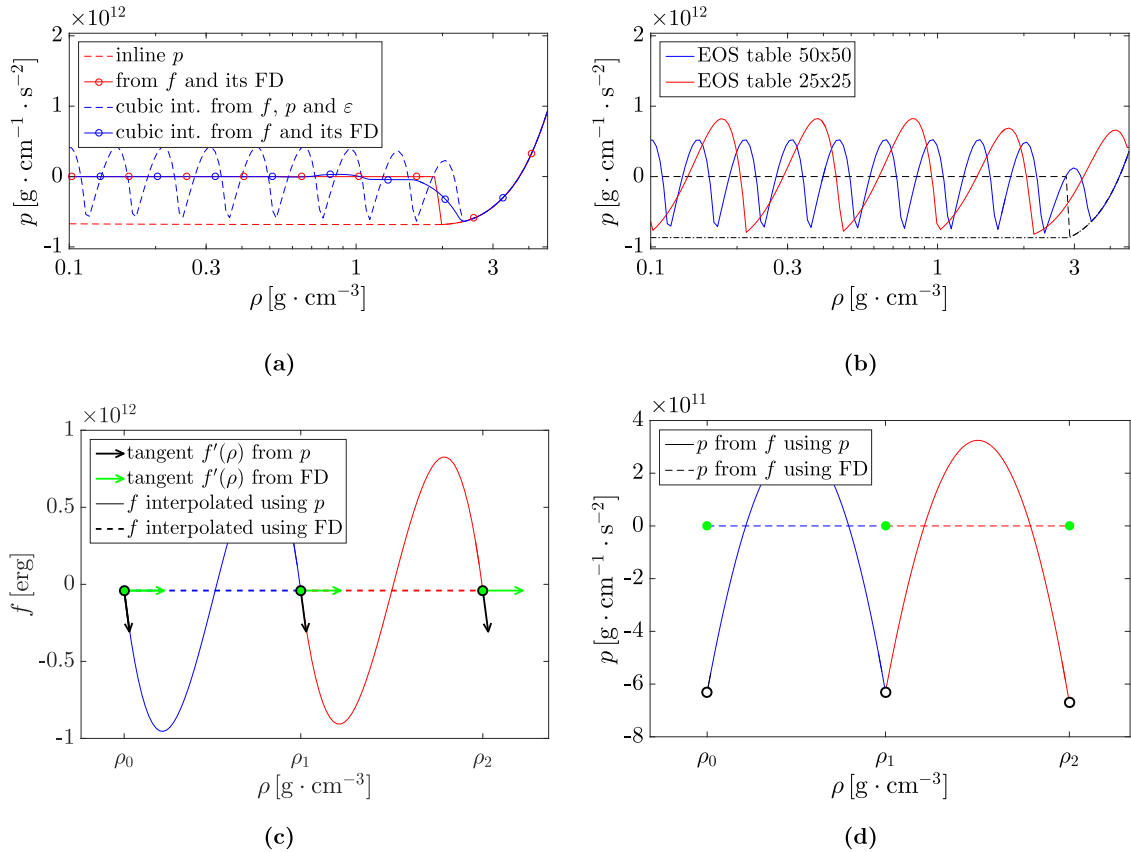


**Fig. 8.** FEOS, inconsistency of variables. Upper row: electron pressure, cut at  $T = 5.5$  eV. (a): bicubic *thermodynamic interpolation* of  $f$  using inline  $p$  and  $\varepsilon$  provides totally wrong pressure, even (b) depending on the density of EOS table data! Dependence of (c) HFE and (d) pressure on density at  $T = 1.6$  eV, using points  $\rho_0 = 2.12\text{e-}3$ ,  $\rho_1 = 2.18\text{e-}3$ ,  $\rho_2 = 2.25\text{e-}3$ .

that the oscillations are caused by the discrepancy between grid data (values and derivatives of HFE), since their wavelength depends on grid spacing.

In Fig. 9 it is observed, that these spurious oscillations appear on a wide region of  $(T-\rho)$  space and that these oscillations are inherent to both pressure and internal energy. There are always regions where  $\frac{\partial p}{\partial \rho} < 0$ , which leads to complex speed of sound and thus, if not further treated, to an unavoidable failure of the simulation.

It is worth mentioning, that pressure obtained from finite differencing provides correct values of the derivative of HFE as is shown in Fig. 8(c). However, a closer look at Fig. 7(b) reveals, that the internal energy calculated by finite differencing exhibits a sign of oscillations, which lead to an unstable EOS and the hydrodynamic simulation crashes.

The same scenario led us to resorting to the bilinear *direct interpolation* of pressure and internal energy in Section 4.3, where the SESAME data are used. Even though the SESAME tables were constructed with a significant care about the thermodynamic consistency, we found a very similar problem as in the case of inline FEOS.

As in the previous case, we can find a certain discordance between the values of pressure/internal energy and the Helmholtz free energy. The appearance of spurious oscillations can be observed also on the discrete data shown in Fig. 10, which presents the dependence of electron pressure (lines without markers), resp. ion pressure (lines with markers) on density at temperature 5.5 eV as obtained from SESAME by bicubic *thermodynamic interpolation* (red, purple), resp. bilinear *direct interpolation* (blue, green). While for electrons the bicubic *thermodynamic interpolation* oscillates, for ions it is not the case here.

A similar issue can also be seen in more detail in Fig. 11. Apparently, both the pressure and the internal energy exhibit serious oscillations when the bicubic *thermodynamic interpolation* is used. The origin of this can be spotted in Fig. 11(c). When observed in more detail, one can see, that the interpolation of HFE correctly matches its discrete values and also its derivatives calculated from pressure. Nevertheless, the condition of HFE increment (31) is apparently violated in the red interval of Fig. 11(c), since both slopes  $f'(\rho_1)$  and  $f'(\rho_2)$  are higher than the slope  $[\rho_1, \rho_2]$ . The oscillation effect appearing in the interpolation of  $f$  in Fig. 11(c), not important at first glance, is however massively amplified in the interpolation of pressure in Fig. 11(d). Unfortunately, it is not only an inappropriate range of pressure but it also possesses thermodynamic qualities ( $\frac{\partial p}{\partial \rho} < 0$ ), which lead to an unstable EOS.



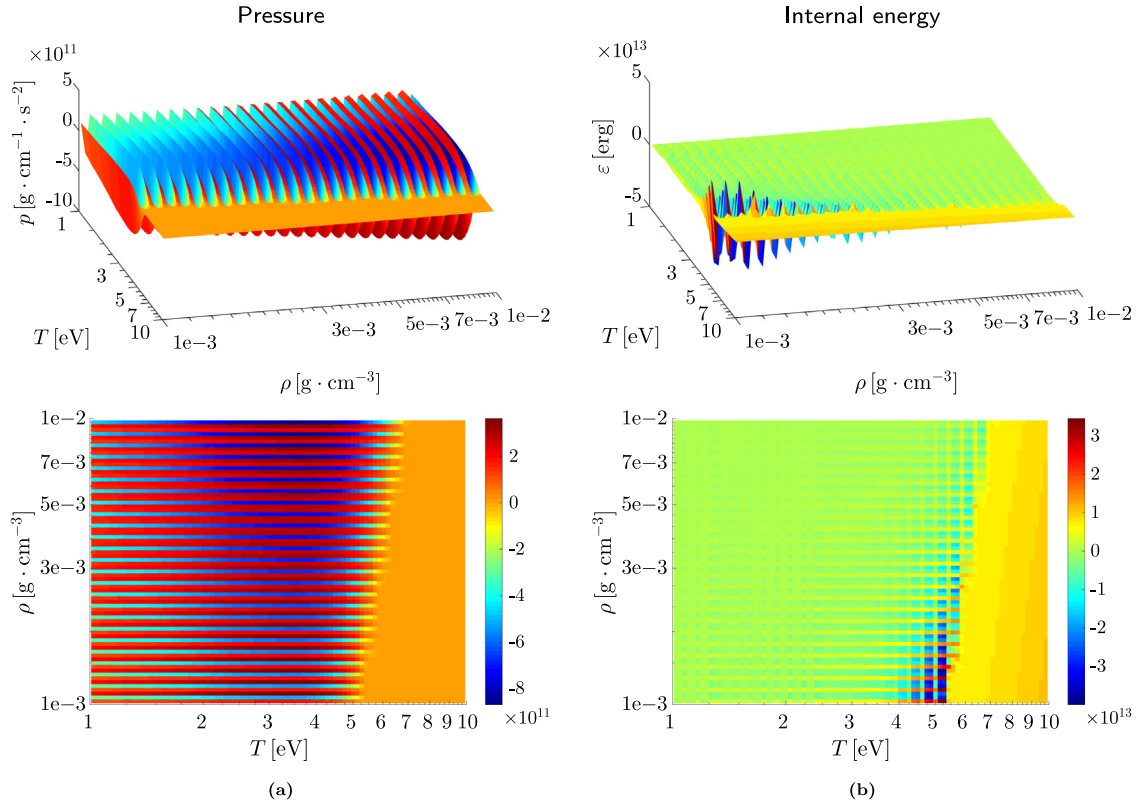


**Fig. 9.** FEOS for electrons in Aluminum, bicubic *thermodynamic interpolation* of HFE from inconsistent data leads to spurious oscillations of (a) pressure and (b) internal energy.

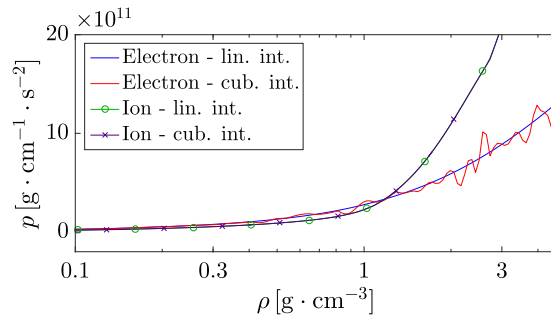


**Fig. 10.** SESAME, electron and ion pressure at  $T = 5.5$  eV by bicubic *thermodynamic interpolation* of HFE and bilinear *direct interpolation*.

In conclusion, in spite of a promising finite difference approach, in the presented tests we did not succeed to use the bicubic *thermodynamic interpolation* for any of the non-trivial inline EOS libraries, since each exhibits some kind of oscillations, either in pressure or in internal energy, thus rendering the resulting quantities thermodynamically unstable. The same also holds for the discrete tabulated quantities and their *thermodynamic interpolation*. Consequently, the standard bilinear *direct interpolation* has been used here as a safe remedy, which can be applied since it avoids the values of HFE.

### 5.2.2. HFE not being a potential

Another issue related to the values of HFE provided by the EOS libraries resides in an essential property of being potential, represented by (16). This requirement should be satisfied by any EOS and in the case of inline EOS libraries it can be checked explicitly by the method of finite differencing. However, the property of HFE of being a potential can be also recast as a relation between pressure and internal energy, represented by (18). This property should be satisfied at any point of  $T$ - $\rho$  space and can be checked for any EOS library, including the tabulated data, where some kind of interpolation is applied. At this point we want to stress once again, that separately constructed *direct interpolations* of pressure and internal energy do

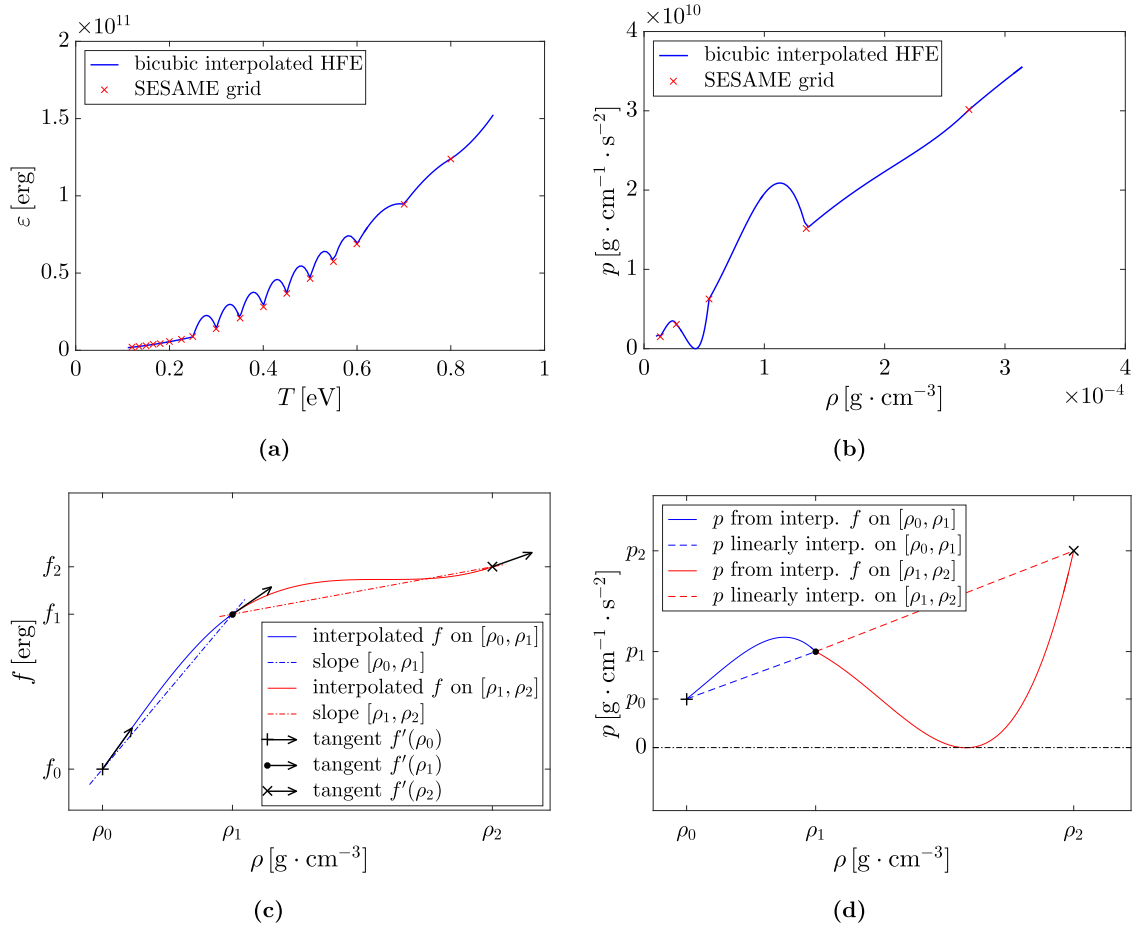


**Fig. 11.** SESAME for electrons in Aluminum. (a) internal energy at  $\rho = 6\text{e} - 5 \text{ g cm}^{-3}$ , (c) HFE at  $T = 250 \text{ eV}$ , (b, d) pressure at  $T = 250 \text{ eV}$ . Lower right plot (d) is a zoom of the left portion of (b) with SESAME interpolation nodes  $\rho_0 = 1.35\text{e} - 5$ ,  $\rho_1 = 2.70\text{e} - 5$ ,  $\rho_2 = 5.40\text{e} - 5$ . (c) is the corresponding HFE. Solid line results from bicubic thermodynamic interpolation of HFE in all plots.

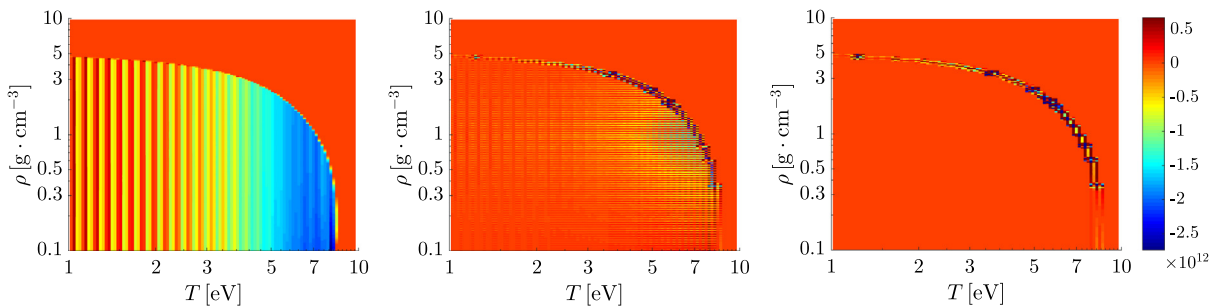


**Fig. 12.** FEOS. Discrepancy  $\text{Err}^{\text{pot}}$ , measuring the violation of the requirement of HFE being a potential. Calculated with inline  $p$  and  $\varepsilon$  (left) and with  $p$  and  $\varepsilon$  obtained from bicubic thermodynamic interpolation of HFE, constructed using inline  $p$  and  $\varepsilon$  (center) or  $p$  and  $\varepsilon$  from finite differencing of inline HFE (right).

not automatically satisfy (18). On the other hand, the potentiality of HFE is guaranteed by the definition of *thermodynamic interpolation* if bicubic or higher order interpolation is applied on consistent data.

Let us now check whether this is the case in practice, that is, whether bicubic *thermodynamic interpolation* ensures that Helmholtz free energy (and consequently also internal energy) is a potential, satisfying (16). In particular, we will check the

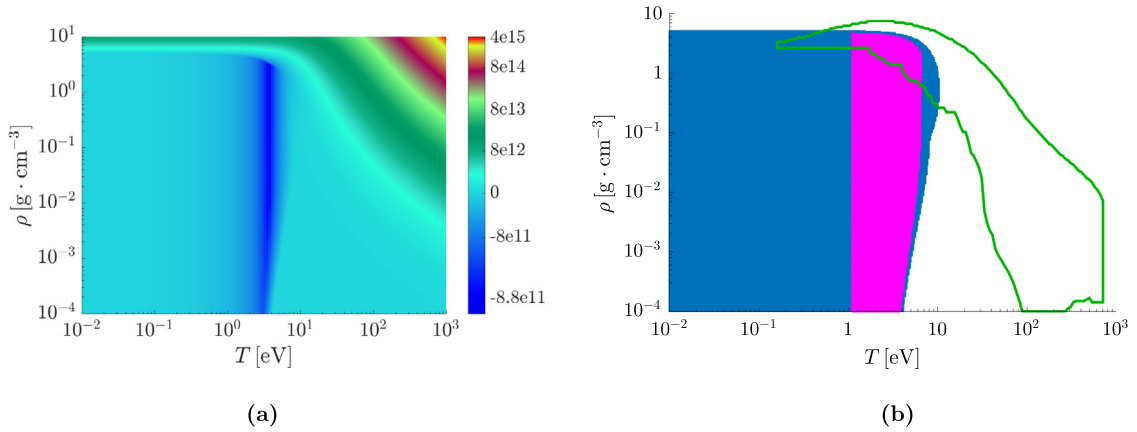


**Fig. 13.** Inline FEOS: electron pressure (a) and regions where it is negative (b). Blue:  $p_e < 0$ , purple:  $p_e < -5 \times 10^{11} \text{ g cm}^{-1} \text{ s}^{-2}$ . (For interpretation of the references to color in this figure legend, the reader is referred to the web version of this article.)

validity of (18) by calculating

$$\text{Err}^{\text{pot}} = p - T \frac{\partial p}{\partial T} - \rho^2 \frac{\partial \varepsilon}{\partial \rho}, \quad (32)$$

where electron pressure and internal energy are obtained in various ways. Fig. 12 shows  $\text{Err}^{\text{pot}}$  as calculated using FEOS with  $p$  and  $\varepsilon$  obtained inline, that is, as the standard user of FEOS is expected to do (left plot), from bicubic *thermodynamic interpolation* of HFE constructed using the inline values of HFE,  $p$  and  $\varepsilon$  (center plot), and from bicubic *thermodynamic interpolation* of HFE constructed using the inline values of HFE and its finite differences (right plot). To assess how serious this “discrepancy of potentiality” expressed by  $\text{Err}^{\text{pot}}$  is, let us recall that the typical pressure in this region is of the same order of magnitude, about  $10^{12} \text{ g cm}^{-1} \text{ s}^{-2}$ , confront Fig. 13(a).

We assume that large absolute values of  $\text{Err}^{\text{pot}}$  are due to the inconsistency of pressure and internal energy in FEOS library resulting from data post-processing or merging of various models, an issue seen earlier e.g. in Fig. 7. The center plot of Fig. 12 looks better, however there are still ripples caused by the inconsistency of  $p$  and  $\varepsilon$  with HFE, which has been also discussed earlier, namely in Section 5.2. This is almost completely cured in the far right plot of Fig. 13, where the values of  $p$  and  $\varepsilon$  provided by FEOS are not used at all, since the *thermodynamic interpolation* is only constructed from HFE and its derivatives, and therefore there cannot be any inconsistency between state variables in provided data. Some violation is still visible along the boundary of the two regions/models inside FEOS.

Similar (but less serious) violation of “potentiality” is observed in the SESAME EOS library, but the situation there is more complicated because there are no inline functions provided to be used for finite differencing. We will not distract the reader by details here.

These observations seem to justify our approach to maintain physical consistency by using higher order of *thermodynamic interpolation*, and actually suggest that it can be used to partially recover consistency in inconsistent data. This will be the subject of further study. In fact, despite all the difficulties described above (and those to be described below), according to our practical experience we are deeply convinced, that the physical consistency gained by the *thermodynamic interpolation* approach is still worth the effort to fix the flaws in EOS data on input, since any neglected principal physical inconsistency, such as HFE not being a potential, will resurface sooner or later during the attempts to further improve the simulation relevancy and precision, or during the extension of the physical model by further phenomena.

### 5.3. Physical irrelevance

It is a well known fact, that a general EOS for hydrodynamic simulation represents an extremely complex problem, and moreover, there is no elegant model being valid on the entire  $(T-\rho)$  domain. Consequently, a set of models needs to be applied, and these models have to be combined appropriately with respect to the values of density and temperature. This can lead to some numerical artifacts or to misuse of the model outside its range of validity, which results in thermodynamically unstable representations of quantities like pressure or internal energy.

A typical case of using the EOS model outside its range of validity, which leads to a negative pressure, is in Fig. 13. (Let us recall that here we want the EOS to provide positive ion and electron pressure. See the remark in Section 2.2 on the possible use of negative electron pressure in the two-temperature model.) Electron pressure as calculated by inline FEOS is shown in Fig. 13(a). Note the logarithmic scaling of temperature and density. The blue patch in Fig. 13(b) highlights the region where pressure values are negative and the purple patch shows its sub-region with electron pressure less than

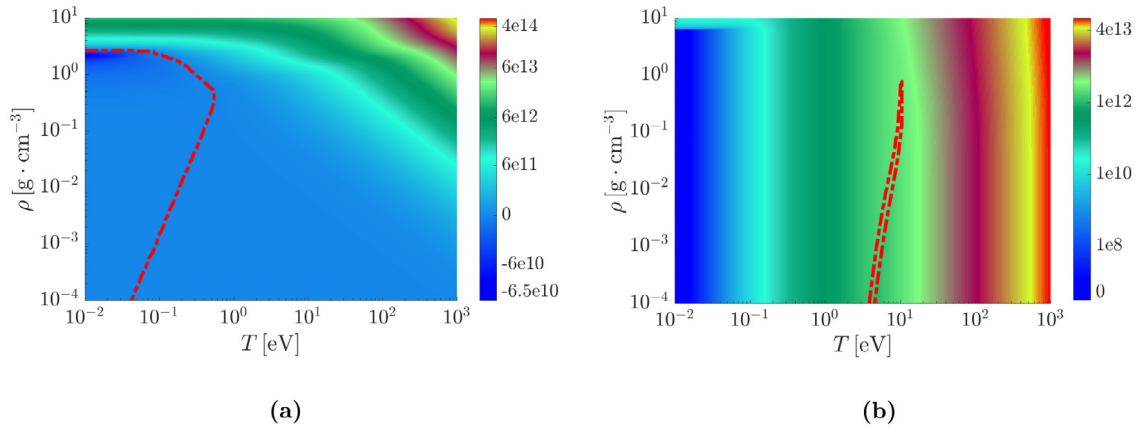


**Fig. 14.** Regions with physical relevancy flaws outlined by dashed red contours. (a) SESAME for Aluminum: negative ion pressure. (b) Inline FEOS for CH plastic: Non-monotonous ion internal energy yields negative heat capacity  $c_V$ . (For interpretation of the references to color in this figure legend, the reader is referred to the web version of this article.)

$-5 \times 10^{11} \text{ g cm}^{-1} \text{ s}^{-2}$ . This is already a serious violation, considering the fact that this is an inline EOS and that typical pressures in our simulation (inside the green contour) are about  $10^{12}$  to  $10^{13} \text{ g cm}^{-1} \text{ s}^{-2}$ .

Similar flaws in physical relevancy can be observed in the case of ions as seen in Fig. 14. Similarly to the FEOS model of electrons, the ion model used in SESAME tables also exhibits a region with negative Aluminum pressure outlined by red dashed contour in Fig. 14(a), where the values have been obtained from the bilinear *direct interpolation* of ion pressure.

The typical effect of a localized violation introduced in Fig. 5(b) is actually present in the ion model of CH provided by FEOS. Such a dip-like structure can be unfortunately observed in the internal energy model of ions. Consequently, there is a thin region possessing a non-monotonous internal energy, outlined by the red dashed contour in Fig. 14(b), resulting in negative heat capacity  $c_V$ . This artifact appears due to the material phase change, i.e., a continuous connection between solid and liquid phases of the material.<sup>2</sup>

To summarize, the issues outlined in this section clearly reveal the fact, that obtaining excellent data from existing Equations of State, both inline and tabulated, is a very difficult (but not impossible) task that requires extra effort in order to provide the simulation with a physically relevant representation of thermodynamic quantities.

## 6. Conclusions and future work

The library HerEOS has been developed for the evaluation of general Equations of State by Hermite-type interpolation, providing some very desirable thermodynamic properties. This tool has been tested with various inline (analytical) and tabulated EOS, and applied in two-temperature hydrodynamic simulations of laser heated plasmas. It has been employed in several multi-dimensional hydrodynamic codes written in Fortran and C++, which exhibits its robustness and independence. In the future we also plan to include an interface for Python. It has been demonstrated that the bicubic and biquintic *thermodynamic interpolations* work well on consistent EOS input. However, some issues related to the thermodynamic consistency have been observed for commonly used EOS libraries, and in such situations a remedy by using the classical bilinear *direct interpolation* is recommended. Let us remark, that even in this case the HerEOS library is still useful as a tool to easily use various Equations of State in various codes (in the inline or interpolated manner).

For tested inline Equations of State a significant reduction of computational cost has been achieved by this approach and even better speed-up is expected in large calculations with more complicated EOS and more state variables employed.

We have demonstrated the usefulness of the *thermodynamic interpolations* approach with consistent EOS. Although the potential of this method is limited by the consistency and the physical relevance of input provided by the particular EOS, we have shown that the general physical properties gained by the *thermodynamic interpolations* approach, such as the preservation of “potentiality”, are worth not giving up. Therefore, future work will focus on the detection and automatic correction of obvious flaws in the source EOS data, utilizing for example machine learning. Other possible paths to be studied include alternative approximation techniques such as surface fitting [23]. As a response to the issues related to the inconsistent values of HFE vs. pressure and internal energy, a new strategy of an automatic construction of HFE (resp. its discrete values) could be useful to improve our *thermodynamic interpolation* approach.

<sup>2</sup> At this point let us remark, that perfection across the phase transition cannot be achieved using only HFE. In fact, one would need to employ also the Gibbs energy, which is not a function of  $(T, \rho)$ . Accounting for it would lead to a more expensive approach. Moreover, Gibbs energy is typically not provided by the EOS libraries. However, we believe that for our purposes the HFE interpolation is sufficient.

## Acknowledgments

The authors would like to thank Pierre-Henri Maire and Jiří Limpouch for fruitful discussions and very helpful comments, John Grove for sharing his tremendous expertise on EOS, and Jan Nikl for his collaboration on the PETE code. Some ideas for the final version of this text emerged during the Shark-FV 2018 Conference in Póvoa de Varzim, Minho, Portugal. The authors also highly appreciate the contribution of both anonymous reviewers, who have carefully read the manuscript and shared their insightful thoughts, which resulted in added explanations, remarks and improvements of the text.

This research was partly supported by the Czech Science Foundation project 18-20962S, the Czech Ministry of Education project RVO 68407700, the project CZ.02.1.01/0.0/0.0/16\_019/0000778 from European Regional Development Fund and the Czech Technical University project SGS16/247/OHK4/3T/14.

## Appendix A. Thermodynamic relations for monoatomic ideal gas

Let us verify that the thermodynamic relations (10)–(14) hold (and see how they look like) for the simple case of a monoatomic ideal gas.

We repeat the well-known equation for pressure

$$p(T, \rho) = \frac{N k_B T}{V(\rho)} = \frac{N k_B T}{\frac{M}{\rho}} = \frac{N k_B T \rho}{N m_a} = \frac{k_B}{m_a} T \rho, \quad (\text{A.1})$$

where  $k_B$  is the Boltzmann constant,  $V(\rho)$  is volume,  $m_a$  the mass of a single atom,  $N$  the number of atoms and  $M = N m_a$  the mass of all atoms. Specific entropy is entropy  $S$  per mass,

$$\begin{aligned} s(T, \rho) = \frac{S}{M} &= \frac{k_B}{m_a} \left( \ln \left[ \frac{V(\rho) T^{\frac{3}{2}}}{N T^{\frac{3}{2}} \left( \sqrt{\frac{h^2}{2\pi m_a k_B T}} \right)^3} \right] + \frac{5}{2} \right) \\ &= \frac{k_B}{m_a} \left( \ln \left[ \frac{m_a}{\rho} \left( \frac{2\pi m_a k_B T}{h^2} \right)^{\frac{3}{2}} \right] + \frac{5}{2} \right), \end{aligned} \quad (\text{A.2})$$

where  $h$  is the Planck constant. Similarly, specific internal energy is internal energy  $U$  per mass,

$$\varepsilon(T, \rho) = \frac{U}{M} = \frac{\frac{3}{2} N k_B T}{N m_a} = \frac{3}{2} \frac{k_B}{m_a} T, \quad (\text{A.3})$$

and the reader can also easily find in literature expressions for the specific isochoric heat capacity

$$c_v(T, \rho) = \frac{3}{2} \frac{k_B}{m_a} \quad (\text{A.4})$$

and the adiabatic speed of sound

$$c_s(T, \rho) = \sqrt{\frac{5}{3} \frac{p}{\rho}} = \sqrt{\frac{5}{3} \frac{k_B T}{m_a}}. \quad (\text{A.5})$$

Now it is only a simple exercise to verify that all these expressions can be obtained by differentiating the specific Helmholtz free energy  $f(T, \rho)$  of monoatomic ideal gas

$$f(T, \rho) = -\frac{k_B T}{m_a} \left( \ln \left[ \frac{m_a}{\rho} \left( \frac{2\pi m_a k_B T}{h^2} \right)^{\frac{3}{2}} \right] + 1 \right) \quad (\text{A.6})$$

and applying thermodynamic relations (10)–(14). For example, pressure from (12) is

$$p(T, \rho) = \rho^2 \left( \frac{\partial f}{\partial \rho} \right)_T = \rho^2 \frac{k_B T}{m_a \rho} = \frac{k_B}{m_a} T \rho, \quad (\text{A.7})$$

which corresponds to (A.1), and the speed of sound from (14) yields

$$\begin{aligned} c_s(T, \rho) &= \sqrt{2\rho \left( \frac{\partial f}{\partial \rho} \right)_T + \rho^2 \left( \frac{\partial^2 f}{\partial \rho^2} \right)_T - \rho^2 \left( \frac{\partial^2 f}{\partial T^2} \right)_\rho^{-1} \left( \frac{\partial^2 f}{\partial T \partial \rho} \right)^2} \\ &= \sqrt{2\rho \frac{k_B T}{m_a \rho} + \rho^2 \left( -\frac{k_B T}{m_a \rho^2} \right) - \rho^2 \left( -\frac{3}{2} \frac{k_B}{m_a T} \right)^{-1} \left( \frac{k_B}{m_a \rho} \right)^2} \\ &= \sqrt{2 \frac{k_B}{m_a} T - \frac{k_B}{m_a} T + \left( \frac{k_B}{m_a} \right)^2 \left( \frac{2}{3} \frac{m_a T}{k_B} \right)} = \sqrt{\frac{5}{3} \frac{k_B}{m_a} T}. \end{aligned} \quad (\text{A.8})$$

Similarly, one can easily verify all the remaining relations, like the dependence of heat capacity and internal energy (13) or the crucial relation (16), resp. (18), proving that HFE is a potential.

## Appendix B. One-dimensional quintic Hermite interpolation

Let us recall how to derive a quintic Hermite interpolation between two points in one dimension. We want to approximate a function  $f(x)$  on interval  $[x_0, x_1]$  by a fifth order polynomial  $\tilde{f}(x)$  such, that the approximating function's values, first and second derivatives at the endpoints  $x_0$  and  $x_1$  agree with those of the original function.

So, denoting the known values

$$\begin{aligned} f^0 &= f(x_0), & f_x^0 &= f'(x_0), & f_{xx}^0 &= f''(x_0), \\ f^1 &= f(x_1), & f_x^1 &= f'(x_1), & f_{xx}^1 &= f''(x_1), \end{aligned} \quad (\text{B.1})$$

we want to construct a function  $\tilde{f}(x)$  that will approximate  $f(x)$  on interval  $[x_0, x_1]$  and satisfy

$$\begin{aligned} \tilde{f}(x_0) &= f^0, & \tilde{f}'(x_0) &= f_x^0, & \tilde{f}''(x_0) &= f_{xx}^0, \\ \tilde{f}(x_1) &= f^1, & \tilde{f}'(x_1) &= f_x^1, & \tilde{f}''(x_1) &= f_{xx}^1. \end{aligned} \quad (\text{B.2})$$

First of all, we map the problem onto interval  $[0, 1]$  using the transformation

$$t = \frac{x - x_0}{x_1 - x_0} \quad (\text{B.3})$$

and then use as a base the Hermite polynomials defined on this interval, so that the approximating function will be of the form

$$\begin{aligned} \tilde{f}(t) &= f^0 H_0(t) + f_x^0 H_1(t)(x_1 - x_0) + f_{xx}^0 H_2(t)(x_1 - x_0)^2 \\ &\quad + f_{xx}^1 H_3(t)(x_1 - x_0)^2 + f_x^1 H_4(t)(x_1 - x_0) + f^1 H_5(t) \end{aligned} \quad (\text{B.4})$$

on  $[0, 1]$  with  $H_i(t)$  being fifth order polynomials on which the boundary conditions (B.2) impose requirements

$$\begin{aligned} H_i(0) &= \delta_{i0}, & (H_i)'(0) &= \delta_{i1}, & (H_i)''(0) &= \delta_{i2}, \\ (H_i)''(1) &= \delta_{i3}, & (H_i)'(1) &= \delta_{i4}, & H_i(1) &= \delta_{i5} \end{aligned} \quad (\text{B.5})$$

for  $i \in \{0, \dots, 5\}$ , with  $\delta_{ij}$  being the Kronecker delta

$$\delta_{ij} = \begin{cases} 1 & \text{for } i = j, \\ 0 & \text{for } i \neq j. \end{cases} \quad (\text{B.6})$$

Hermite polynomials of given order can be found in literature, but they can be also easily derived directly. For example, consider  $H_3(t)$ . We look for a fifth order polynomial, so it will have the form

$$H_3(t) = A + Bt + Ct^2 + Dt^3 + Et^4 + Ft^5 \quad (\text{B.7})$$

and the conditions (B.5) require that

$$H_3(0) = (H_3)'(0) = (H_3)''(0) = H_3(1) = (H_3)'(1) = 0, \quad (H_3)''(1) = 1. \quad (\text{B.8})$$

Values and derivatives of (B.7) at the endpoints are

$$\begin{aligned} H_3(0) &= A, & H_3(1) &= A + B + C + D + E + F, \\ (H_3)'(0) &= B, & (H_3)'(1) &= B + 2C + 3D + 4E + 5F, \\ (H_3)''(0) &= 2C, & (H_3)''(1) &= 2C + 6D + 12E + 20F. \end{aligned} \quad (\text{B.9})$$

Inserting this into boundary conditions (B.8) yields the linear system

$$\begin{pmatrix} 1 & 0 & 0 & 0 & 0 & 0 \\ 0 & 1 & 0 & 0 & 0 & 0 \\ 0 & 0 & 2 & 0 & 0 & 0 \\ 1 & 1 & 1 & 1 & 1 & 1 \\ 0 & 1 & 2 & 3 & 4 & 5 \\ 0 & 0 & 2 & 6 & 12 & 20 \end{pmatrix} \begin{pmatrix} A \\ B \\ C \\ D \\ E \\ F \end{pmatrix} = \begin{pmatrix} 0 \\ 0 \\ 0 \\ 0 \\ 0 \\ 1 \end{pmatrix} \quad (\text{B.10})$$

with the solution  $A = B = C = 0, D = F = 1/2, E = -1$ , so that this base polynomial is

$$H_3(t) = \frac{1}{2}t^3 - t^4 + \frac{1}{2}t^5. \quad (\text{B.11})$$



Similar systems are solved for the other conditions, so that we get the complete set of quintic Hermite base polynomials

$$\begin{aligned} H_0(t) &= 1 - 10t^3 + 15t^4 - 6t^5, & H_3(t) &= \frac{1}{2}t^3 - t^4 + \frac{1}{2}t^5, \\ H_1(t) &= t - 6t^3 + 8t^4 - 3t^5, & H_4(t) &= -4t^3 + 7t^4 - 3t^5, \\ H_2(t) &= \frac{1}{2}t^2 - \frac{3}{2}t^3 + \frac{3}{2}t^4 - \frac{1}{2}t^5, & H_5(t) &= 10t^3 - 15t^4 + 6t^5. \end{aligned} \quad (\text{B.12})$$

Now the quintic Hermite interpolation function (B.4) is completely defined. Let us remark, that in practical calculations one can also use the symmetry w.r.t. the interval midpoint  $t = 1/2$ , that is,

$$\begin{aligned} H_5(t) &= H_0(1-t), \\ H_4(t) &= H_1(1-t), \\ H_3(t) &= H_2(1-t). \end{aligned} \quad (\text{B.13})$$

The derivation of a biquintic interpolation, that is, extension of this process to two dimensions, is more lengthy but fully analogous.

## References

- [1] R.M. More, K.H. Warren, D.A. Young, G.B. Zimmerman, A new quotidian equation of state (QEOS) for hot dense matter, *Phys. Fluids* 31 (10) (1988) 3059–3078, <http://dx.doi.org/10.1063/1.866963>.
- [2] S. Faik, A. Tauschwitz, I. Iosilevskiy, The equation of state package FEOS for high energy density matter, *Comp. Phys. Commun.* 227 (2018) 117–125, <http://dx.doi.org/10.1016/j.cpc.2018.01.008>.
- [3] S.P. Lyon, J.D. Johnson, SESAME: The Los Alamos National Laboratory equation of state database, Tech. Rep. LA-UR-92-3407, Los Alamos National Laboratory, Los Alamos, NM, USA, 1992.
- [4] A.J. Kemp, J. Meyer-ter Vehn, An equation of state code for hot dense matter, based on the QEOS description, *Nucl. Instrum. Methods Phys. Res. A* 415 (3) (1998) 674–676, [http://dx.doi.org/10.1016/S0168-9002\(98\)00446-X](http://dx.doi.org/10.1016/S0168-9002(98)00446-X).
- [5] T.A. Heltemes, G.A. Moses, BADGER v1.0: A Fortran equation of state library, *Comput. Phys. Comm.* 183 (12) (2013) 2629–2646, <http://dx.doi.org/10.1016/j.cpc.2012.07.010>.
- [6] R. Liska, M. Kuchařík, J. Limpouch, O. Renner, P. Váchal, L. Bednárik, J. Velechovský, ALE method for simulations of laser-produced plasmas, in: J. Fořt, J. Fürst, J. Halama, R. Herbin, F. Hubert (Eds.), *Finite Volumes for Complex Applications VI - Problems & Perspectives*. FVCA 6, International Symposium, Prague, June 6–10, 2011. Vol. 2, in: *Springer Proceedings in Mathematics*, vol. 4, Springer, 2011, pp. 57–72, [http://dx.doi.org/10.1007/978-3-642-20671-9\\_87](http://dx.doi.org/10.1007/978-3-642-20671-9_87).
- [7] M. Holec, J. Limpouch, R. Liska, S. Weber, High-order discontinuous Galerkin nonlocal transport and energy equations scheme for radiation hydrodynamics, *Int. J. Numer. Methods Fluids* 83 (10) (2017) 779–797, <http://dx.doi.org/10.1002/fld.4288>.
- [8] M. Holec, J. Nikl, S. Weber, Nonlocal transport hydrodynamic model for laser heated plasmas, *Phys. Plasmas* 25 (3) (2018) 032704, <http://dx.doi.org/10.1063/1.5011818>.
- [9] F.D. Swesty, Thermodynamically consistent interpolation for equation of state tables, *J. Comput. Phys.* 127 (1) (1996) 118–127, <http://dx.doi.org/10.1006/jcph.1996.0162>.
- [10] F.X. Timmes, F.D. Swesty, The accuracy, consistency, and speed of an electron-positron equation of state based on table interpolation of the Helmholtz free energy, *Astrophys. J. Suppl. Ser.* 126 (2) (2000) 501–516, <http://dx.doi.org/10.1086/313304>.
- [11] G.I. Kerley, Rational function method of interpolation, Tech. Rep. LA-6903-MS, Los Alamos Scientific Laboratory, Los Alamos, NM, USA, 1977.
- [12] P.R. Levashov, K.V. Khishchenko, I.V. Lomonosov, V.E. Fortov, Database on shock-wave experiments and equations of state available via internet, in: *Shock Compression of Condensed Matter*, in: *AIP Conference Proceedings*, vol. 706, American Institute of Physics, 2004, pp. 87–90, <http://dx.doi.org/10.1063/1.1780190>, database available online at <http://teos.ficp.ac.ru/rusbank/>.
- [13] S. Gavriluk, personal communication, 2018.
- [14] V.A. Dobrev, Tz. V. Kolev, R.N. Rieben, High-order curvilinear finite element methods for Lagrangian hydrodynamics, *SIAM J. Sci. Comput.* 34 (5) (2012) B606–B641, <http://dx.doi.org/10.1137/120864672>.
- [15] M. Fajardo, P. Audebert, P. Renaudin, H. Yashiro, R. Shepherd, J.C. Gauthier, C. Chenaïs-Popovics, Study of the ion-distribution dynamics of an Aluminum laser-produced plasma with picosecond resolution, *Phys. Rev. Lett.* 86 (7) (2001) 1231–1234, <http://dx.doi.org/10.1103/PhysRevLett.86.1231>.
- [16] K. Falk, M. Holec, C.J. Fontes, C.L. Fryer, C.W. Greeff, H.M. Johns, D.S. Montgomery, D.W. Schmidt, M. Smid, Measurement of preheat due to nonlocal electron transport in warm dense matter, *Phys. Rev. Lett.* 120 (2) (2017) 025002, <http://dx.doi.org/10.1103/PhysRevLett.120.025002>.
- [17] K. Falk, E.J. Gamboa, G. Kagan, D.S. Montgomery, B. Srinivasan, P. Tzeferacos, J.F. Benage, Equation of state measurements of warm dense Carbon using laser-driven shock and release technique, *Phys. Rev. Lett.* 112 (15) (2014) 155003, <http://dx.doi.org/10.1103/PhysRevLett.112.155003>.
- [18] K. Falk, C.L. Fryer, E.J. Gamboa, C.W. Greeff, H.M. Johns, D.W. Schmidt, M. Smid, J.F. Benage, D.S. Montgomery, X-ray Thomson scattering measurement of temperature in warm dense Carbon, *Plasma Phys. Controlled Fusion* 59 (1) (2017) 014050, <http://dx.doi.org/10.1088/0741-3335/59/1/014050>.
- [19] K. Falk, L.A. Collins, E.J. Gamboa, G. Kagan, J.D. Kress, D.S. Montgomery, B. Srinivasan, P. Tzeferacos, J.F. Benage, Combined X-ray scattering, radiography, and velocity interferometry/streaked optical pyrometry measurements of warm dense Carbon using a novel technique of shock-and-release, *Phys. Plasmas* 21 (5) (2014) 056309, <http://dx.doi.org/10.1063/1.4876613>.
- [20] K. Falk, S.P. Regan, J. Vorberger, B.J.B. Crowley, S.H. Glenzer, S.X. Hu, C.D. Murphy, P.B. Radha, A.P. Jephcoat, J.S. Wark, D.O. Gericke, G. Gregori, Comparison between X-ray scattering and velocity-interferometry measurements from shocked liquid Deuterium, *Phys. Rev. E* 87 (4) (2013) 043112, <http://dx.doi.org/10.1103/PhysRevE.87.043112>.
- [21] P.M. Celliers, D.K. Bradley, G.W. Collins, D.G. Hicks, T.R. Boehly, W.J. Armstrong, Line-imaging velocimeter for shock diagnostics at the OMEGA laser facility, *Rev. Sci. Instrum.* 75 (11) (2004) 4916, <http://dx.doi.org/10.1063/1.1807008>.
- [22] J.E. Miller, T.R. Boehly, A. Melchior, D.D. Meyerhofer, P.M. Celliers, J.H. Eggert, D.G. Hicks, C.M. Sorce, J.A. Oertel, P.M. Emmel, Streaked optical pyrometer system for laser-driven shock-wave experiments on OMEGA, *Rev. Sci. Instrum.* 78 (3) (2007) 034903, <http://dx.doi.org/10.1063/1.2712189>.
- [23] J. Grove, personal communication, 2017.